Ternary nanocomposite of molybdenum disulfide, reduced graphene oxide and poly(3,4-ethylenedioxythiophene) for supercapacitor

2.1 Introduction

As discussed in the introduction chapter, electrochemical energy storage systems are of paramount importance in modern society. Rechargeable batteries and supercapacitors are two widely investigated electrochemical energy storage systems. Initial work on supercapacitors generally made use of RuO_2. Later, different types of material were investigated as electrode material for supercapacitors. Few examples are MoS_2, WS_2, Cu_2O, ZnO, cellulose fiber, rGO, $ZnCo_2O_4$, PANI, polypyrrole, PEDOT, α-Fe_2O_3, carbon-nanotube, nickel nitride (Ni_3N), VN/MoS_2 hybrids etc. [1-12]. For large scale commercial production, easy and cost effective synthesis methods are required to obtain the electrode materials. Therefore, it is essential to develop new electrode materials and new strategies for achieving energy efficient and higher self-life supercapacitors.

Two-dimensional layered MoS_2 has found application as supercapacitor electrode for their unique structural and electronic properties [13, 14]. MoS_2 structure is basically made up of S-Mo-S sandwiched monolayers which interact via weak van der Waals forces. The layered configuration allows easy intercalation of guest ions such as H^+, Li^+, Na^+, K^+, NH^{4+} providing a scope for interlayer charge storage [15]. Additionally, the central atom Mo in the sandwiched structure possesses various oxidation states from +4 to +6. However, the electronic conductivity of MoS_2 is insufficient for supercapacitor electrodes. The poor electrical conductivity of MoS_2-based supercapacitors can be mitigated by using carbon based conductive materials. Graphene is great conductive material for energy storage devices [14, 16, 17]. Reduced graphene oxide (rGO) is an important material since it has very high electrical conductivity (6000 Scm^{-1}), surface area (up to 2675 m^2g^{-1}) and mechanical strength (~1 T Pa) [18]. However, graphene undergoes serious agglomeration both during preparation and applications. Therefore, the storage behavior of graphene is lower than the expected value. Another material of interest is conducting polymers (CP) which have emerged as highly promising pseudocapacitive materials and offers higher capacity. However, it has relatively poor cycling stability. The poor cycle life

of pseudocapacitive material could be improved by incorporating EDLC material. The composites of CPs with inorganic materials (carbon material, metal oxides) or organic materials show better performances for supercapacitor applications. rGO is the favourable candidate for combination with CP. The agglomeration of rGO could be alleviated by constructing heterostructures with MoS_2. Kim et al. [19] prepared MoS_2/WS_2 heterostructures for enhanced hydrogen evaluation reactions and He et al. [20] synthesized graphene/metallic MoS_2 nanosheet heterostructures by hydrothermal process. Therefore, it is expected that preparation of ternary nanocomposites of MoS_2-rGO with conducting polymer may able improve supercapacitor performances.

Poly(3,4-ethylenedioxythiophene), also known as PEDOT, is regarded as one of the most stable conducting polymers. It possesses high conductivity and it has stabilized oxidation states between benzoid and quinoid [21, 22]. But, the slow rate of ion diffusion during the electrochemical measurements minimizes the efficiency of PEDOT based supercapacitors and therefore development of nanostructures with higher surface area and shorter ion diffusion paths is highly recommended [23].

Therefore, fabrication of electrode materials which can give stable cycling performance, enhanced surface area, improved electrode/electrolyte interaction is required for achieving high energy and high power density supercapacitor. In this context, ternary nanocomposite of PEDOT nanoparticles (PEDOTNPs) with 2D-2D MoS_2-rGO (layer-by-layer) structures bears significance. This chapter deals with the electrochemistry of ternary nanocomposites of PEDOTNPs, MoS_2 and rGO. MoS_2-rGO layer-by-layer structures were prepared by self-assembly method using positively charged MoS_2 and negatively charged GO nanosheets followed by a hydrothermal reduction. PEDOTNPs, MoS_2/PEDOTNPs and rGO/PEDOTNPs nanocomposites were also synthesized for comparison. Further, electrochemical characteristics of MoS_2-rGO/PEDOTNPs// MoS_2-rGO/PEDOTNPs symmetric supercapacitors were investigated.

2.2 Experimental

2.2.1 Materials: Graphite flake (Sigma-Aldrich), molybdenum disulphide flake (MoS_2, Sigma-Aldrich), iron Chloride ($FeCl_3$, Sigma-Aldrich), 3,4-Ethylenedioxythiophene monomer (98%) (EDOT, Sigma-Aldrich), sodium bis(2-ethylhexyl) sulfosuccinate (AOT, Sigma-Aldrich), sulfuric acid (H_2SO_4, avantor), cetyltrimethyl ammonium bromide (CTAB, Hi-media), potassium permanganate

($KMnO_4$, Merck Emplura) and phosphoric acid (H_3PO_4, avantor) were used in various steps of synthesis procedure.

2.2.2 Synthesis of MoS_2-rGO structure: MoS_2 nanosheets were prepared by exfoliating bulk MoS_2 powder in 1% CTAB containing water solution using ultra-sound for 11 h in a water-bath sonicator (36 W) [24]. The suspension was centrifuged at 7000 rpm followed by vacuum drying at desiccator. The measured surface charge of exfoliated MoS_2 is +28 mV as observed from Zeta potential measurement. Positively charged MoS_2 nanosheets were mixed in double distilled (DD) water at the concentration of 1 $mgml^{-1}$. Graphite oxide (GO) was synthesized from raw graphite flakes using improved hummer's method and the as prepared GO was dissolved in DD water at concentration of 1 $mgml^{-1}$ [25]. Graphene oxide (GO after sonication) nanosheets exhibited surface charge of -32.1 mV in zeta potential measurement. MoS_2-rGO nanocomposites were prepared by slowly adding 50 ml of GO suspension into 50 ml of exfoliated MoS_2 suspension under vigorous magnetic stirring. Addition of both the suspensions left greenish brown feathery precipitate at the bottom of the reaction vessel. The obtained precipitate was MoS_2-GO layer-by-layer structures. MoS_2-rGO layer-by-layer structures were obtained after drying MoS_2-GO using freeze drier for 24 h followed by annealing at 200 ^oC for 12 h.

2.2.3 Synthesis of MoS_2-rGO/PEDOTNPs ternary nanocomposite: PEDOTNPs were synthesized with reverse emulsion polymerization method of EDOT monomer in the presence of 250 mM sodium bis(2-ethylhexyl) sulfosuccinate (AOT) micelles and 5 M ferric chloride solution [26]. Freeze dried MoS_2-GO structures were dispersed in DD water using ultrasound for 15 min. Pre-synthesized PEDOTNPs (40 wt %) were added at this stage followed by ultrasonication. The obtained black colored dispersion was transferred into a teflon coated autoclave and annealed at 200 ^oC for 12 h for *in-situ* reduction. *In-situ* reduction of GO was carried out in presence of MoS_2 and PEDOTNPs. M Devi et al. [27] prepared reduced graphene oxide-polypyrrole (rGO-PPy) composites from *in-situ* chemical reduction of GO in the presence of PPy. Huang et al. [28] reported hydrothermally reduced graphene oxide in autoclave. In general, solvent in subcritical or supercritical condition is exposed to the treating material in hydrothermal treatment [29]. The deoxygenation processes of GO are accelerated by compressed water [30]. The hydrogen ions of the compressed water

initiate the reduction process by eliminating -OH groups. Ether and epoxide linkages also form in the GO skeleton in the reduction process by eliminating water. Epoxide groups get reduced to hydroxyl functionalities under hydrothermal conditions. The remaining hydroxyl groups of GO with adjacent hydrogen atoms could reduce to alkene by eliminating water molecules. Thus, the oxygen functional groups of GO could be eliminated in hydrothermal method. The obtained product was washed with DD water and ethanol for several times. rGO/PEDOTNPs and MoS_2/PEDOTNPs nanocomposites were also prepared by maintaining 40 wt% ratio between PEDOTNPs and rGO/MoS_2.

2.2.4 Structural and morphological Characterizations: Powder X-ray diffraction (P-XRD) was carried out in D8 focus X-ray diffractometer, Bruker AXS, Germany (make). Zeta potential was measured in Malvern Zetasizer Nano series, Nano ZS90. Morphology was investigated with Scanning Electron Microscope (SEM) at 20 kV accelerating voltage using JEOL, JAPAN, JSM 6390LV and Transmission Electron Microscopy (TEM) at 60-200 KV in 50 V steps in JEM-2100. Field emission scanning electron microscope (FESEM) images have been performed using Carl Zeiss: ∑IGMA instrument. Raman spectroscopy has been performed with EZ Raman Enwave Optronics spectrometer using 633 nm excitation wavelengths. Brunauere-Emmette-Teller (BET) and contact angle measurements were performed in nova software installed quantachrom instrument and GmbH contact angle measurement system Data physics instrument, respectively. Thermal stability measurements were evaluated in thermogravimetric analyzer of Perkin Elmer under constant N_2 flow in heating rate of 30 ^oC/min. X-ray Photoelectron Spectroscopy (XPS) has been carried out in ESCALAB Xi^+ XPS Microprobe with monochromatic AlKαX-ray source.

2.2.5 Electrochemical measurements: Cyclic voltammetry (CV), galvanostatic charge/ discharge (GCD) and electrochemical impedance spectroscopy (EIS) measurements were investigated in three electrodes and two electrodes arrangement in AUTOLAB Potentiostat/ Galvanostat 302N Modular and FRA32M, Netherlands at room temperature. The three electrodes were: 3 M saturated KCl electrolyte filled Ag/AgCl (reference electrode), platinum rod (3 mm, counter electrode) and Ni foam pressed with active material (working electrode). Working electrodes were produced by ultrasonicating active material, carbon black and nafion in 85:10:5 mass ratios in

DD water. The obtained slurry was coated onto a piece of Ni foam (2x0.5 cm^2), pressed at 10 MPa, and finally dried at desiccator. Mass of the active material deposited on each electrode was measured from 1 mg to 1.5 mg. The CV and GCD were carried out in 3 M KOH aqueous electrolyte at a potential window of -0.3 V to 0.6 V and EIS was recorded in AUTO FRA modular within the frequency range of 10^7 to 0.001 Hz.

Specific capacitance (C_{sp}) was calculated with the equation no [2.1]:

$$C_{sp} = \frac{I \times \Delta T_d}{m \times \Delta V} \quad [2.1]$$

where $I, \Delta T_d, m \; and \; \Delta V$ are discharge current, discharge period, mass of the active material and potential drop of discharge period.

Two electrode measurements were performed in a symmetric assembly of MoS_2-rGO/PEDOTNPs electrodes (MoS_2-rGO/PEDOTNPs // MoS_2-rGO/PEDOTNPs). Assembled MoS_2-rGO/PEDOTNPs // MoS_2-rGO/PEDOTNPs symmetric supercapacitors were tested for CV and GCD measurements in 3 M KOH aqueous electrolyte. Cycling stability of MoS_2-rGO/PEDOTNPs // MoS_2-rGO/PEDOTNPs symmetric supercapacitors was carried out for 10,000 cycles at 20 Ag^{-1} of current density. Specific capacitance (C_{sp}), specific energy (E) and specific power (P) of the symmetric supercapacitor are evaluated with following equations:

$$\text{Specific capacitance, } C_{sp} = \frac{4 \times I \times \Delta T_{dis}}{m \times \Delta V} \quad [2.2]$$

$$\text{Specific energy, } E = \frac{1}{8} C_{sp} (\Delta V)^2 \quad [2.3]$$

$$\text{Specific power, } P = \frac{E \times 3600}{\Delta T_{dis}} \quad [2.4]$$

where, C_{sp}, $\Delta V, m, I$ and ΔT_{dis} are the discharged specific capacitance, potential window of discharge, loaded mass of active material, discharge current and discharge duration, respectively.

2.3. Results and discussion

2.3.1 Schematic representation: The synthesis procedure of ternary MoS_2-rGO/PEDOTNPs nanocomposites have been explained schematically in scheme 2.I. Step (a) of scheme 2.I depicts the exfoliation of MoS_2 in presence of CTAB (zeta potential = +28 mV). Step (b) explains the preparation of graphene oxides from graphite oxide (zeta potential = -32.1 mV). Fabrication of MoS_2-GO layer-by-layer

structures has been explained in step (c) and final fabrication step of ternary MoS_2-rGO/PEDOTNPs nanocomposites is shown in step (d).

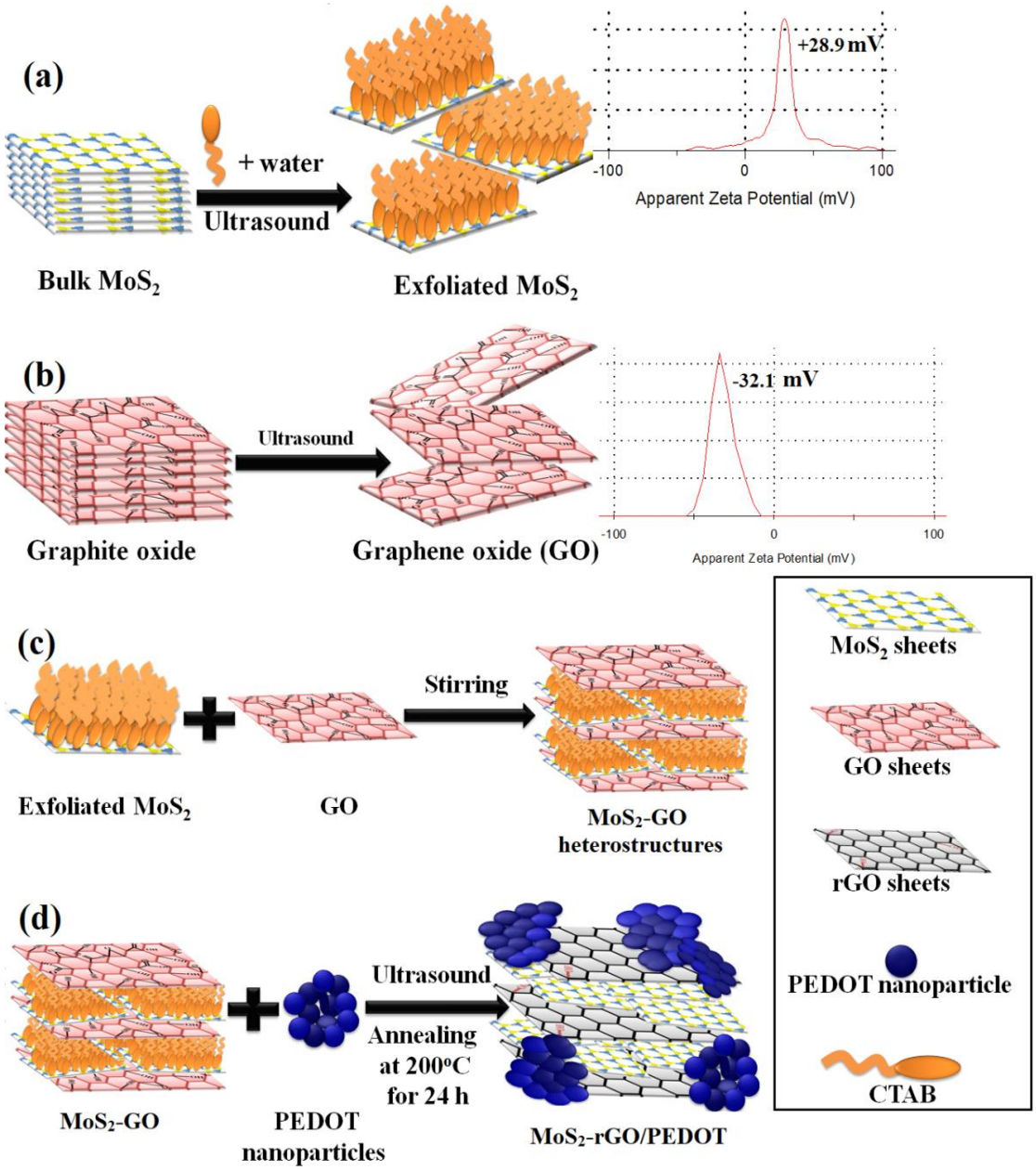

Scheme 2.I: Schematic of synthesis steps of ternary MoS_2-rGO/PEDOTNPs nanocomposites. (a) Exfoliation of MoS_2, (b) graphite oxide to graphene oxide, (c) MoS_2-GO layer-by-layer structures, and (d) ternary MoS_2-rGO/PEDOTNPs nanocomposites by *in-situ* reduction.

2.3.2 X-ray diffraction analysis: XRD patterns of bulk MoS_2, exfoliated MoS_2, reduced graphite oxide (rGO) and MoS_2-rGO layer-by-layer structures are shown in

Figure 2.1 (a) and PEDOTNPs, rGO/PEDOTNPs, MoS_2/PEDOTNPs and MoS_2-rGO/PEDOTNPs are displayed in Figure 2.1 (b). Standard XRD pattern of MoS_2 possesses many crystalline phases (JCPDS no. 77-1716) (Figure 2.1 a (i)) and peaks are centered at $2\theta = 14.3^o(002)$, $29.04^o(004)$, $32.65^o(100), 33.51^o(101)$, $35.82^o(102)$, 39.58^o (103), $44.16^o(106)$, $44.2^o(104)$, $49.83^o(105)$, 56.04^o (106), 58.35^o (110). After the liquid phase exfoliation of MoS_2 with cationic surfactant CTAB the XRD peaks disappeared except the peak corresponding to (002) plane. The intensity of that peak has decreased much. The smaller intensity and increased FWHM of the XRD peak for (002) plane suggests successful exfoliation of MoS_2. The standard XRD card of graphite (JCPDS no. 75-2078) is shown in Figure 2.1 (iv) of which the peaks are centred at $2\theta = 26.61^o$, 43.45^o, 46.32^o and 54.81^o. XRD pattern of rGO exhibits peaks at $2\theta = 25.02^o$ and $2\theta = 42.97^o$ suggesting removal of functional groups of GO nanosheets. MoS_2-rGO nanocomposite exhibits XRD peak at $2\theta = 19.3^o$ attributed that the characteristic peak of rGO ($2\theta = 25.02^o$) has shifted to lower diffraction angle. This suggests intercalation of MoS_2 layers in-between rGO layers and the formation of MoS_2-rGO layer-by-layer structures. XRD pattern of PEDOTNPs shows a broad hump at around 26^o (020) (Figure 2.1b) which is the characteristic signature of amorphous conducting polymers [31]. The XRD peak at around 12.5^o of PEDOTNPs is attributed to the 2D stacking pattern of polymer chain [32]. XRD pattern of MoS_2/PEDOTNPs nanocomposite also shows the broad characteristic hump of PEDOTNPs and a small peak for exfoliated MoS_2 at around 14^o. Similarly, XRD hump of rGO/PEDOTNPs is attributed to the superposition of (020) plane of PEDOTNPs and (002) plane of rGO. XRD pattern of ternary MoS_2-rGO/PEDOTNPs nanocomposite exhibits the same broad hump at arround $2\theta = 17^o - 30^o$ (Figure 2.1 b). The characteristic MoS_2 peak is missing in the XRD pattern of the ternary nanocomposite which may be attributed to the shifting of diffraction peak towards lower diffraction angle upon rGO intercalation and also PEDOTNPs prevents the random restacking of MoS_2 nanosheets.

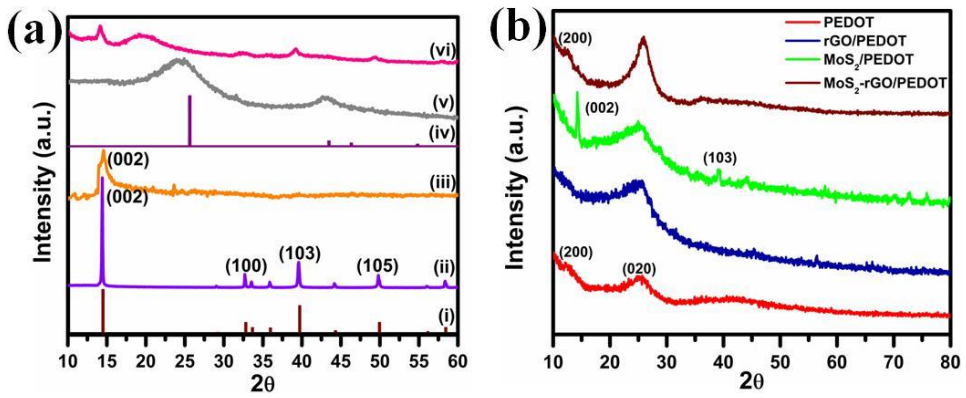

Figure 2.1: XRD of (a) standard patterns of MoS_2 (JCPDS no. 77-1716) (i), bulk MoS_2 (ii), Exfoliated MoS_2 (iii), standard patterns of graphite (JCPDS no. 75-2078) (iv), reduced graphene oxide (rGO) (v), and MoS_2-rGO layer-by-layer structures (vi); (b) PEDOTNPs, rGO/PEDOTNPs, MoS_2/PEDOTNPs and MoS_2-rGO/PEDOTNPs nanocomposites.

2.3.3 Morphological analysis (Scanning electron microscope and Transmission electron microscope): SEM micrographs of bulk and exfoliated MoS_2 have been taken to understand the peeling effect and displays in Figure 2.2 (a-d). Compactly packed layered structures are clearly observed for commercially available bulk MoS_2 flakes (Figure 2.2 a, b) with lateral size of 1 to 5 µm and thickness of few hundred nanometer. After liquid phase exfoliation by sonication, the lateral size of the MoS_2 sheets has been observed in the range of 200 nm to 500 nm (Figure 2.2 c, d). The changes in surface morphology in terms of lateral size and thickness of the nanosheets also suggest successful peeling of bulk MoS_2.

The morphology and nanostructures of as-prepared MoS_2-rGO layer-by-layer structures were investigated with scanning electron microscope (SEM) and transmission electron microscope (TEM) (Figure 2.3 (a-d)). TEM images of exfoliated MoS_2 nanosheets and rGO nanosheets are shown in Figure 2.3 (a) and (b), respectively. Pure rGO nanosheets are observed to be agglomerated (Figure 2.3 b) and inset shows the rGO nanosheets at higher magnification. More detail information of MoS_2-rGO layer-by-layer structures is obtained from TEM micrograph shown in Figure 2.3 (c, d) where MoS_2 nanosheets are distinguished on the top of rGO nanosheets (Figure 2.3c) and below of which some layered structures is observed.

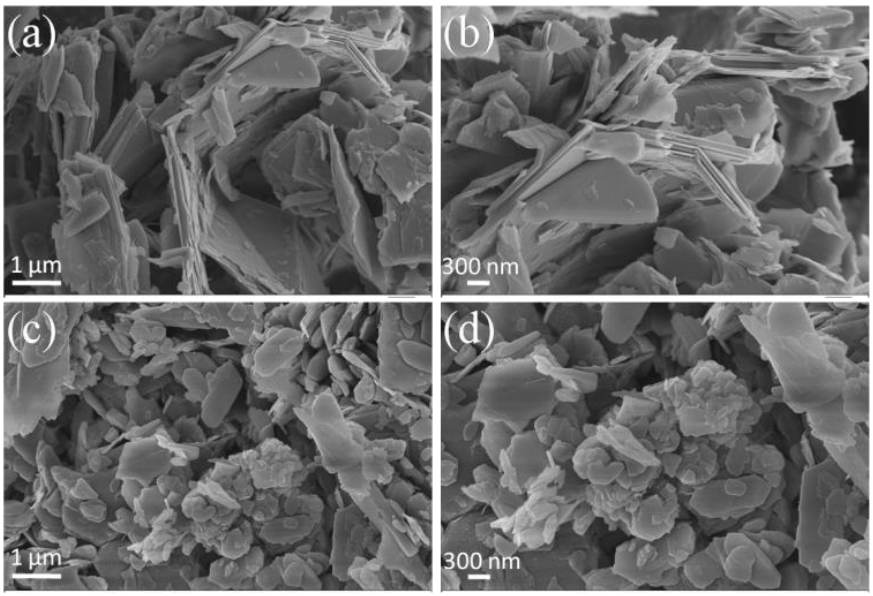

Figure 2.2: FESEM micrographs of (a, b) bulk MoS_2, (c, d) exfoliated MoS_2

In Figure 2.3 (d), MoS_2 nanosheet is noted over large rGO nanosheet, suggesting the successful formation of MoS_2-rGO structures. SEM micrograph of MoS_2-rGO is depicted in Figure 2.3 (e). Loosely bound layer-by-layer structures are observed for MoS_2-rGO nanocomposite. The edges of the 2D nanosheets are rolled up attributed to the general characteristic of graphene. The energy-dispersive X-ray spectroscopy (EDX) mapping of MoS_2-rGO layer-by-layer structures are displayed in Figure 2.3 (f). Mapping depicts the homogeneous distribution of Mo, S, C and O throughout the layered structures.

Thereafter, SEM micrographs of synthesized PEDOTNPs and ternary MoS_2-rGO/PEDOTNPs nanocomposites are shows in Figure 2.4 a, b. Overall, particle type of morphology has been observed for PEDOTNPs (Figure 2.4 a). PEDOTNPs have covered the MoS_2-rGO layer-by-layer structures in ternary nanocomposites (Figure 2. 4 b) and at some portions the layered structures are visible below the PEDOTNPs.
Ternary MoS_2-rGO/PEDOTNPs nanocomposites have been investigated with EDX spectroscopy (Figure 2.4 c) and quantitative analysis suggests the presence of 62.37 wt% of C, 36.5 wt% of O, 0.73 wt% of S and 0.29 wt% of Mo.

Further, more detailed morphology of the synthesized PEDOTNPs, rGO/PEDOTNPs, MoS_2/PEDOTNPs and ternary MoS_2-rGO/PEDOTNPs nanocomposites were investigated with TEM (Figure 2.5 (a-f)). Agglomerated

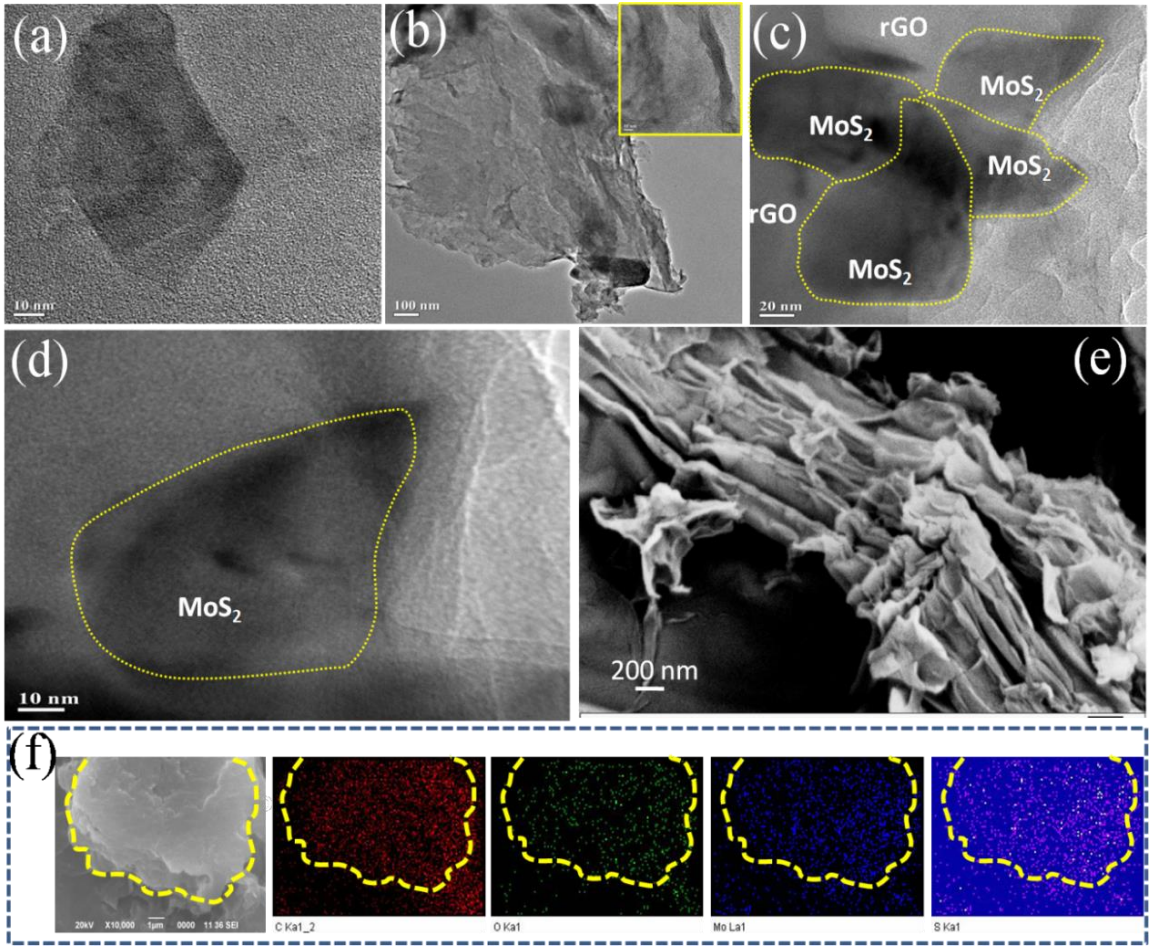

Figure 2.3: TEM micrographs, (a) MoS_2 nanosheets, (b) rGO nanosheets (inset shows rGO nanosheets at higher magnification), (c) and (d) MoS_2-rGO layer-by-layer structures at different magnifications, (e) SEM micrograph of rGO-MoS_2 layer-by-layer structures, and (f) elemental mapping of C, O, Mo and S in MoS_2-rGO.

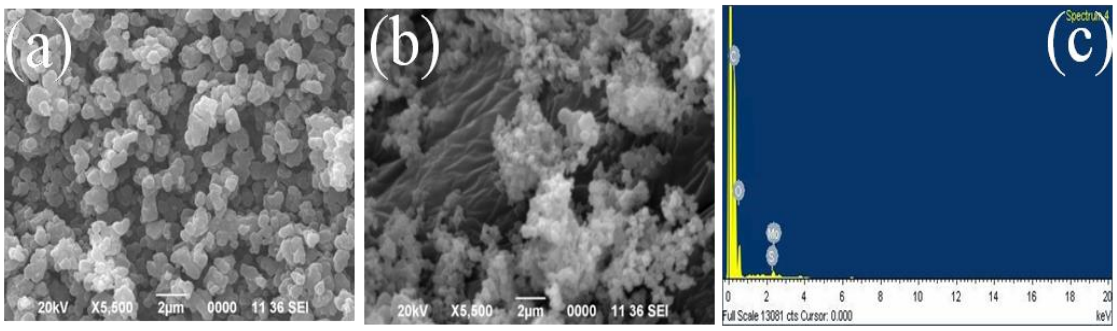

Figure 2.4: SEM micrographs, (a) PEDOTNPs, (b) MoS_2-rGO /PEDOTNPs ternary nanocomposites, (c) EDX of MoS_2-rGO /PEDOTNPs ternary nanocomposites.

PEDOTNPs are observed in Figure 2.5 (a), possessing an average diameter of 154 nm. A single PEDOTNP can be located in Figure 2.5 (b). The morphology of

rGO/PEDOTNPs nanocomposites is shown in Figure 2.5 (c) where paper like rGO nanosheets is observed with PEDOTNPs. The rGO nanosheets are quite agglomerated as observe from the TEM micrographs in the binary nanocomposites. PEDOTNPs are noticed to be dispersed on MoS_2 nanosheets in binary MoS_2/PEDOTNPs nanocomposites as noted from Figure 2.5 (d). TEM micrograph of ternary MoS_2-rGO/PEDOTNPs nanocomposites clearly shown the layer-by-layer arrangements

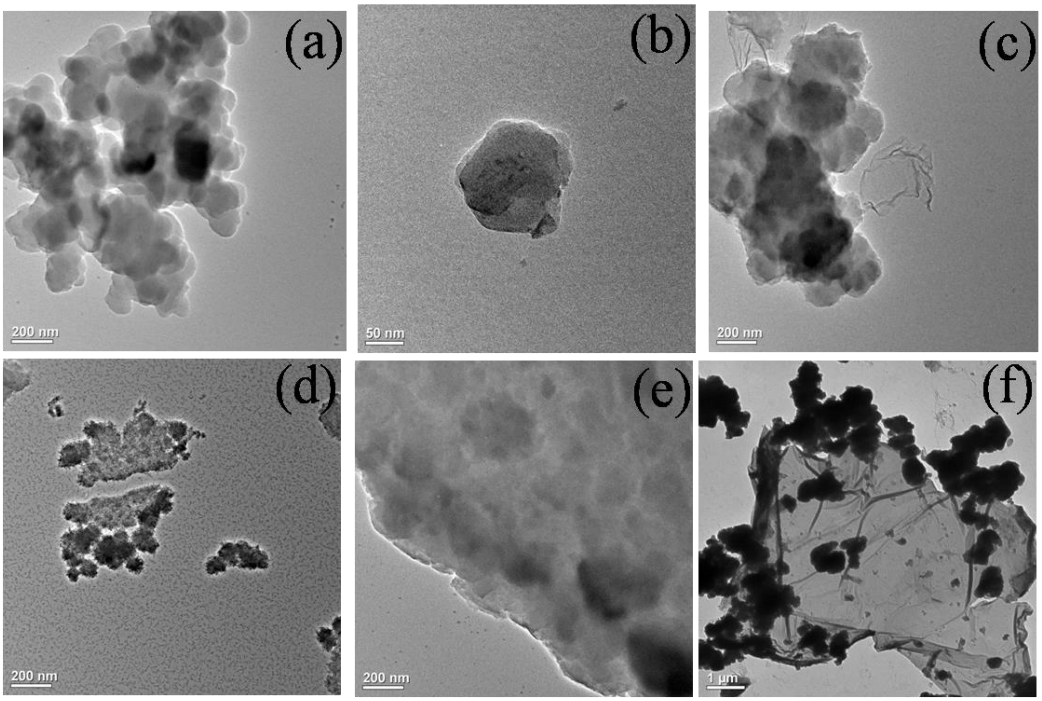

Figure 2.5: TEM micrographs of (a) and (b) PEDOTNPs, (c) rGO/PEDOTNPs nanocomposite, (d) MoS_2/PEDOTNs nanocomposite, and (e) and (f) MoS_2-rGO /PEDOTNPs ternary nanocomposites at different magnifications.

of 2D nanosheets on which PEDOTNPs are dispersed (Figure 2.5e). Figure 2.5f displays the large nanosheets of rGO-MoS_2 layer-by-layer structures with the nano-particles for the ternary nanocomposite. Higher bending modulus of MoS_2 prevents the agglomeration of rGO in the rGO-MoS_2 layer-by-layer structures and as a result of which large rGO nanosheets can be seen without agglomeration in MoS_2-rGO/PEDOTNPs ternary nanocomposites providing larger surface area and interfaces which may be beneficial for improving the charge storage.

2.3.4 Thermogravimetric (TG) analysis: Thermal properties of synthesized PEDOTNPs, rGO/PEDOTNPs, MoS_2/PEDOTNPs and MoS_2-rGO/PEDOTNPs

ternary nanocomposites have been studied with TG analysis in the temperature range of 50 ^{o}C to 800 ^{o}C. The experiments were performed in nitrogen environment at a heating rate of 20 ^{o}/min. Figure 2.6 a shows the TG curves of MoS_2, rGO, PEDOTNPs, rGO/PEDOTNPs, MoS_2/PEDOTNPs and MoS_2-rGO/PEDOTNPs. TG pattern of bulk MoS_2 is completely stable upto 475 ^{o}C. The degradation slope of bulk MoS_2 from 475 ^{o} to 650 ^{o}C ascribes to conversion of MoS_2 to MoO_3 [33]. For the other materials, degradation around 100 ^{o}C is due to the removal of surface absorbed water. TG curve of rGO shows 20-30% of degradation in the temperature range of 250 ^{o}C - 350 ^{o}C attributes to the degradation of unstable oxygen containing functional groups of rGO such as, hydroxyl, epoxy etc. [34]. PEDOTNPs show continuous degradation slope started at 273 ^{o}C and degrades almost 88% at 800 ^{o}C, ascribes to the burning of polymer chain [31]. rGO/PEDOTNPs nanocomposites show 79% of weight loss

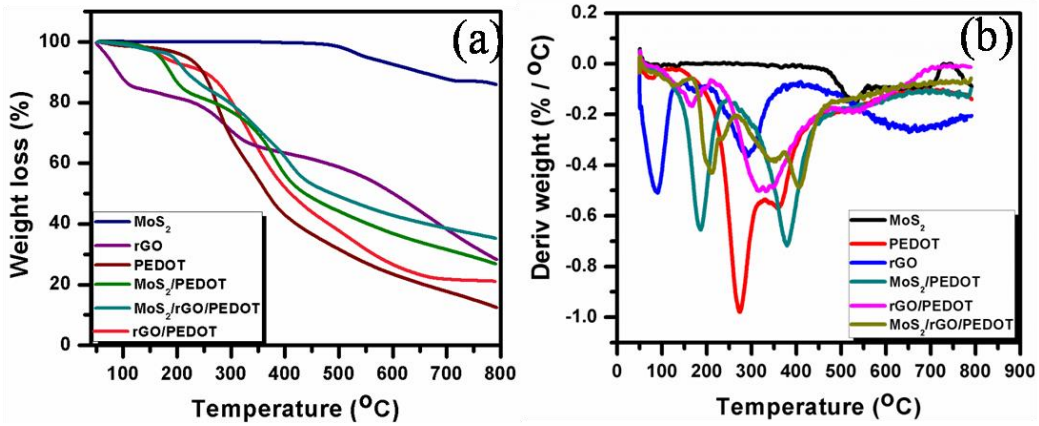

Figure 2.6: (a) TG analysis and (b) derivative of weight loss curves with temperature of MoS_2, rGO, PEDOTNPs, rGO/PEDOTNPs, MoS_2/PEDOTNPs and MoS_2-rGO/PEDOTNPs nanocomposites.

and MoS_2/PEDOTNPs show 74% of weight loss at 800 ^{o}C as observed from respective TG curves. Ternary MoS_2-rGO/PEDOTNPs nanocomposites possess 15-40% of degradation within the temperature range of 250 ^{o}C - 425 ^{o}C and finally exhibit 35% of thermal stability at 800 ^{o}C. Degradation slopes observed in the temperature range of 372-519 ^{o}C for rGO, rGO/PEDOTNPs and MoS_2-rGO/PEDOTNPs nanocomposites are attributed to the burning of carbon ring of graphene [35]. Better thermal stability of the ternary nanocomposites ascribes to the presence of highly stable MoS_2 and rGO nanosheets and interaction between them.

Table 2.1: Obtained values of onset decomposition temperature (T_{onset}), rapidest decomposition temperature (T_{rpd}) and degradation % at 800 ^oC from TG analysis and derivative of weight loss curves

Sample code	Onset decomposition Temperature T_{onset} (^oC)	Rapidest decomposition Temperature T_{rpd} (^oC)	% of degradation at 800^oC
MoS_2	469	530	14%
rGO	438	662	72%
PEDOTNPs	170	273	88%
MoS_2/PEDOTNPs	260	380	74%
rGO/PEDOTNPs	230	328	79%
MoS_2-rGO/PEDOTNPs	268	410	65%

Derivative of weight loss with temperature of MoS_2, rGO, PEDOTNPs, rGO/PEDOTNPs, MoS_2/PEDOTNPs and MoS_2-rGO/PEDOTNPs have been plotted to measure the onset decomposition (T_{onset}) and rapidest decomposition (T_{rpd}) of nanocomposites. Derivative TG curves are shown in Figure 2.6 b and measured T_{onset} and T_{rpd} values with total weight loss at 800 ^oC are summarized in Table 2.1. Derived TG curves of PEDOTNPs, rGO/PEDOTNPs, MoS_2/PEDOTNPs and MoS_2-rGO/PEDOTNPs show at least two peaks arise due to water molecules and polymer chain, respectively. T_{onset} and T_{rpd} for rGO/PEDOTNPs nanocomposite have increased after incorporation of rGO with measured values of T_{onset}= 230 ^oC and T_{rpd}= 328 ^oC while PEDOTNPs possesses T_{onset}= 170 ^oC and T_{rpd}= 273 ^oC. Incorporation of MoS_2-rGO structures in PEDOTNPs matrix further stabilizes the ternary nanocomposites than that of binary composites with T_{onset}= 268 ^oC and T_{rpd}= 410 ^oC.

2.3.5 Raman analysis: To investigate the molecular morphology and vibrational and rotational energy states of PEDOTNPs, rGO/PEDOTNPs, MoS_2/PEDOTNPs and MoS_2-rGO/PEDOTNPs ternary nanocomposites, Raman spectra have been recorded

to compare and displayed in Figure 2.7 (i-iii). Sharp characteristic peaks of PEDOTNPs (Figure 2.7 i a) appear at 1330 cm^{-1}, 1430 cm^{-1} and 1538 cm^{-1} are

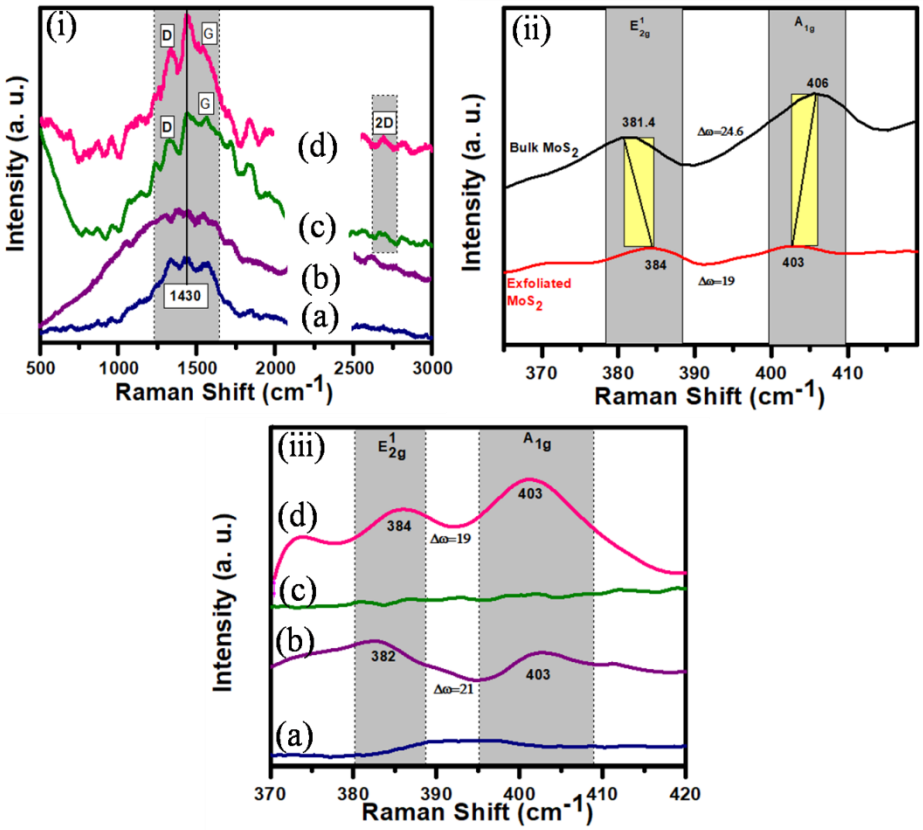

Figure 2.7: Raman Spectra, (i) (a) PEDOTNPs, (b) MoS_2/PEDOTNPs, (c) rGO/PEDOTNPs and (d) MoS_2-rGO/PEDOTNPs; (ii) bulk and exfoliated MoS_2; and (iii) (a) PEDOTNPs, (b) MoS_2/PEDOTNPs, (c) rGO/PEDOTNPs and (d) MoS_2-rGO/PEDOTNPs nanocomposites.

assigned to C_β-C_β stretching deformations, C_α=C_β symmetrical stretching vibration, asymmetrical C_α=C_β stretching vibration associated with the thiophene rings of polymer chain, respectively [36]. The other band of PEDOTNPs at 1258 cm^{-1} is due to C_α–C_α inter-ring stretching mode, 990 cm^{-1} is due to oxyethylene ring deformation mode, 697 cm^{-1} is due to C–S–C symmetric deformation mode, 571 cm^{-1} is due to C-O-C bond deformation mode [37]. Figure 2.7 i b shows the Raman spectrum of MoS_2/PEDOTNPs nanocomposites. The Raman feature appears at around 1333 cm^{-1} and 1580 cm^{-1} for rGO/PEDOTNPs (Figure 2.7 i c) and MoS_2-rGO/PEDOTNPs (Figure 2.7 i d) are corresponding to D and G bands of graphene. The G peak is due to the doubly degenerated zone center E_{2g} mode whereas D band appears for defected graphene. Figure 2.7 ii compares the Raman spectra of bulk and exfoliated MoS_2.

Both E_{2g}^1 and A_{1g} modes of MoS_2 are observed around 381 cm^{-1} and 406 cm^{-1}, respectively for bulk and exfoliated MoS_2. E_{2g}^1 mode is ascribed to the in-plane vibrations of sulphur atoms towards Mo in the trilayer MoS_2 and A_{1g} mode is attributed to the out-of-plane vibrations of sulphur atoms in the opposite direction. It is observed that frequency of A_{1g} mode decreases (red shift) and E_{2g}^1 mode increases (blue shift) for exfoliated MoS_2 than that of bulk MoS_2. The interlayer van der Waals force suppresses atomic vibration in MoS_2 when the layer numbers is more, resulting in higher force constants [38]. In the other words, moving from monolayer to bulk MoS_2, A_{1g} mode stiffen and E_{2g}^1 mode soften suggesting that long-range interlayer Coulombic interactions in multilayer MoS_2 or stacking induced structure changes may dominate the change of atomic vibration rather than interlayer van der Waals force [39]. The bulk MoS_2 possesses a peak separation between E_{2g}^1 and A_{1g} modes of 24.5 cm^{-1} where as for the exfoliated MoS_2 the peak separation is 19 cm^{-1}. Figure 7 iii displays the E_{2g}^1 and A_{1g} peak positions of the synthesized nanocomposites.

2.3.6 X-ray Photoelectron Spectroscopy analysis: X-ray Photoelectron Spectroscopy **(**XPS) survey spectra of pure PEDOTNPs, MoS_2-rGO and MoS_2-rGO/PEDOTNPs ternary nanocomposites are shown in Figure 2.8 (a). High resolution C1s XPS spectrum of PEDOTNPs indicates the presence of C=C bonds, C=C-O bonds and C-O bonds attributed to the peaks located at 284.7 eV, 285.9 eV and 287.7 eV, respectively (Figure 2.8 b) [40, 41]. O1s spectrum (Figure 2.8 c) of PEDOTNPs is deconvoluated into two peaks centered at 531.3 eV and 533 eV arises from the oxygen bonded with either sulphur or carbon and C-O-C=O groups, respectively. The sulfur high resolution spectrum (S2p) of PEDOTNPs has been deconvoluated into six peaks (Figure 2.8 d) attributed to neutral sulfur (163.6 eV and 166 eV), cationic sulfur (167.2 eV and 168.2 eV) and oxidized sulfur (169.2 eV and 179.7 eV), corroborating with the previous report [42]. The electrons in $2p_{1/2}$ and $2p_{3/2}$ doublet spectra give the sulfur signal in the region of 163-168 eV associated with sulfur atoms of the thiophene rings of PEDOTNPs and the oxidized sulfur signal may arise due to the exposure into air [43].

The atomic and elemental analysis of MoS_2-rGO structures and the valence states have been understood with the XPS spectra of MoS_2-rGO. Mo3d high resolution spectrum is observed for MoS_2 in MoS_2-rGO structures and depicted in Figure 2.8 e. The strong binary signals at 229.6 eV and 232.7 eV suggest Mo^{4+} $3d_{3/2}$

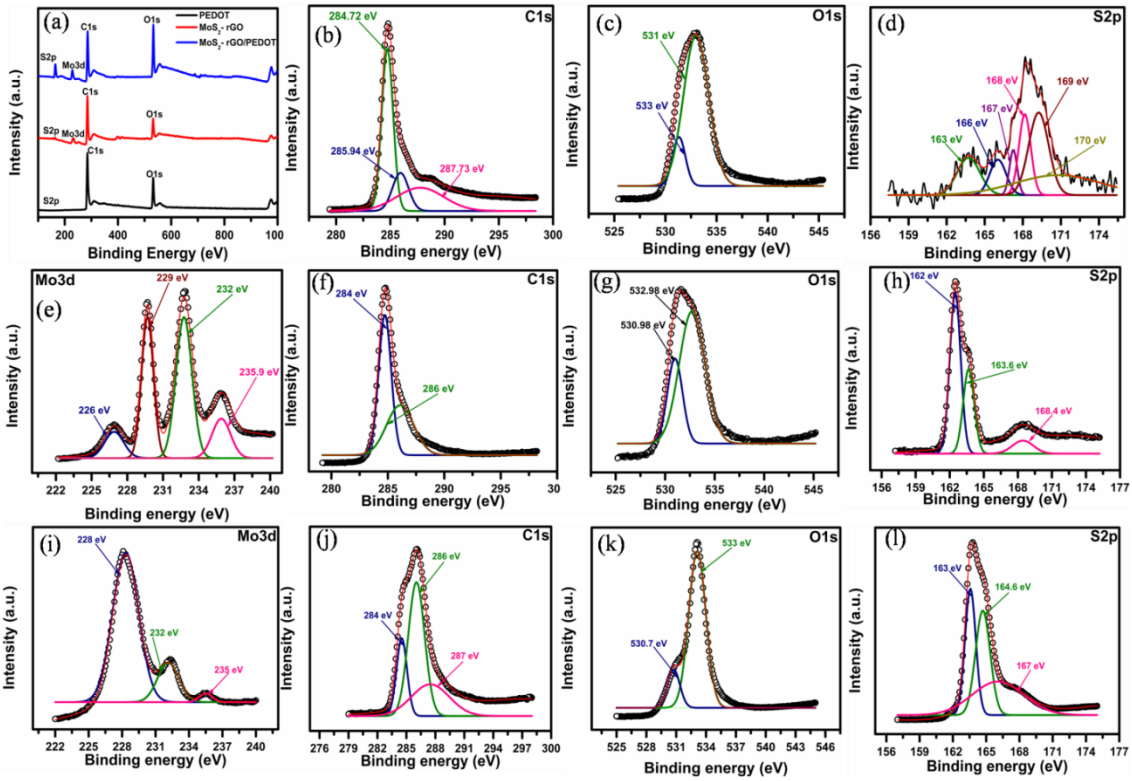

Figure 2.8: XPS spectra of PEDOTNP, MoS_2-rGO layer-by-layer structures, and MoS_2-rGO/PEDOTNPs ternary nanocomposites. (a) Survey spectra of PEDOTNPs, MoS_2-rGO, and MoS_2-rGO/PEDOTNPs, (b) C1s profile of PEDOTNPs, (c) O1s profile of PEDOTNPs, (d) S2p profile of PEDOTNPs, (e) Mo3d profile of MoS_2-rGO layer-by-layer structures, (f) C1s profile of MoS_2-rGO layer-by-layer structures, (g) O1s profile of MoS_2-rGO layer-by-layer structures, (h) S2p profile of MoS_2-rGO layer-by-layer structures, (i) Mo3d profile of MoS_2-rGO/PEDOTNPs ternary nanocomposites, (j) C1s MoS_2-rGO/PEDOTNPs profile of ternary nanocomposites, (k) O1s profile of MoS_2-rGO/PEDOTNPs ternary nanocomposites, and (f) S2p profile of MoS_2-rGO/PEDOTNPs ternary nanocomposites.

and Mo^{4+} $3d_{5/2}$ states of Mo with 3.1 eV spin orbit splitting in MoS_2-rGO structures [44]. Another oxidation state of molybdenum i.e. Mo^{5+} is located from the fitted peak centered at 235.9 eV which may appear due to the strong interaction of Mo with the oxygen functional groups of rGO in MoS_2-rGO layer-by-layer structures [45]. Figure 2.8 e also carries S2p peak located at 226.9 eV suggesting the presence S in MoS_2 [46]. C1s spectrum of MoS_2-rGO layer-by-layer structures is consisted of two fitted peaks (Figure 2.8 f) centered at 284.7 eV and 286.1 eV which are assigned for sp2

hybridized carbon atoms and C-OH (epoxy/hydroxy) groups of rGO, respectively [47].

Further, 530.9 eV peak in the O profile (Figure 2.8 g) discloses the non-stoichiometry of O may attribute to partial attachment of O with S of MoS_2 suggesting S-rGO interaction i.e. interaction between S and rGO lattice and confirms the formation of MoS_2-rGO layer-by-layer structures. The other peak centered at 532.7 eV in high resolution O spectrum is related to surface attached oxygen groups of rGO. Moreover, high resolution S2p spectra have also been analyzed (Figure 2.8 h) to understand the S profile with the fitted peaks located at 162.4 eV, and 163.6 eV associated with S $2p_{3/2}$ and S $2p_{1/2}$ spin-orbit coupling of S of MoS_2 [48]. Another broad peak centered at 168.4 eV located in S profile ascribes C-S interaction suggesting the interaction between S of MoS_2 and C of rGO in MoS_2-rGO structures.

The wide scan survey spectrum of MoS_2-rGO/PEDOTNPs discloses the co-existence of Mo, S, C and O in ternary nanocomposite as shown in Figure 2.8 a. In the Mo 3d profile also (Figure 2.8i), the peaks are appearing at 228.4 eV, 232.1 eV and 235.5 eV owing to Mo^{4+} $3d_{3/2}$, Mo^{4+} $3d_{5/2}$ and Mo^{5+} states, respectively. Deconvoluated C1s peaks (Figure 2.8 j) are appearing at 284.5 eV, 286 eV and 287.5 eV attributed to sp2 hybridized C atoms, C-OH bonds and C-O bonds, respectively. O profile (Figure 2.8 k) of the ternary nanocomposite implies the interaction between S-rGO, rGO-PEDOTNPs due to the appearance of peak at 530.7 eV and 533.1 eV, respectively. Deconvoluated S 2p peak (Figure 2.8 l) shows peaks at 163.5 eV, 164.6 eV and 167.2 eV corresponding to S $2p_{3/2}$, S $2p_{1/2}$ and C-S bonding, respectively.

2.3.7 Specific surface area and porosity analysis: To measure the specific surface area and to understand the nature of pores present in PEDOTNPs, rGO/PEDOTNPs, MoS_2/PEDOTNPs and MoS_2-rGO/PEDOTNPs nanocomposites, N_2-adsorption-desorption experiment has been carried at 77 K. The resulting isotherms are illustrated in Figure 2.9 (a-d). The isotherms of all the nanocomposites describe gradual N_2-uptake followed by sharp increase at the end. These are type IV isotherms and high absorption capacity at medium relative pressure (0.4-0.9) indicates the presence of significant amount of mesopores in PEDOTNPs, rGO/PEDOTNPs, MoS_2/PEDOTNPs and MoS_2-rGO/PEDOTNPs nanocomposites. The desorption isotherms of all the nanocomposites are associated with a hysteresis loop, classified as type H4 hysteresis. Hysteresis phenomena of the BET isotherms are associated with

capillary condensation and multilayer adsorption in mesoporous interior. The BET specific surface area for rGO/PEDOTNPs (264 m^2g^{-1}) and MoS_2/PEDOTNPs (219 m^2g^{-1}) are larger than that of PEDOTNPs (167 m^2g^{-1}). The ternary MoS_2-rGO/PEDOTNPs nanocomposites exhibit the highest specific surface area of 528 m^2g^{-1}.

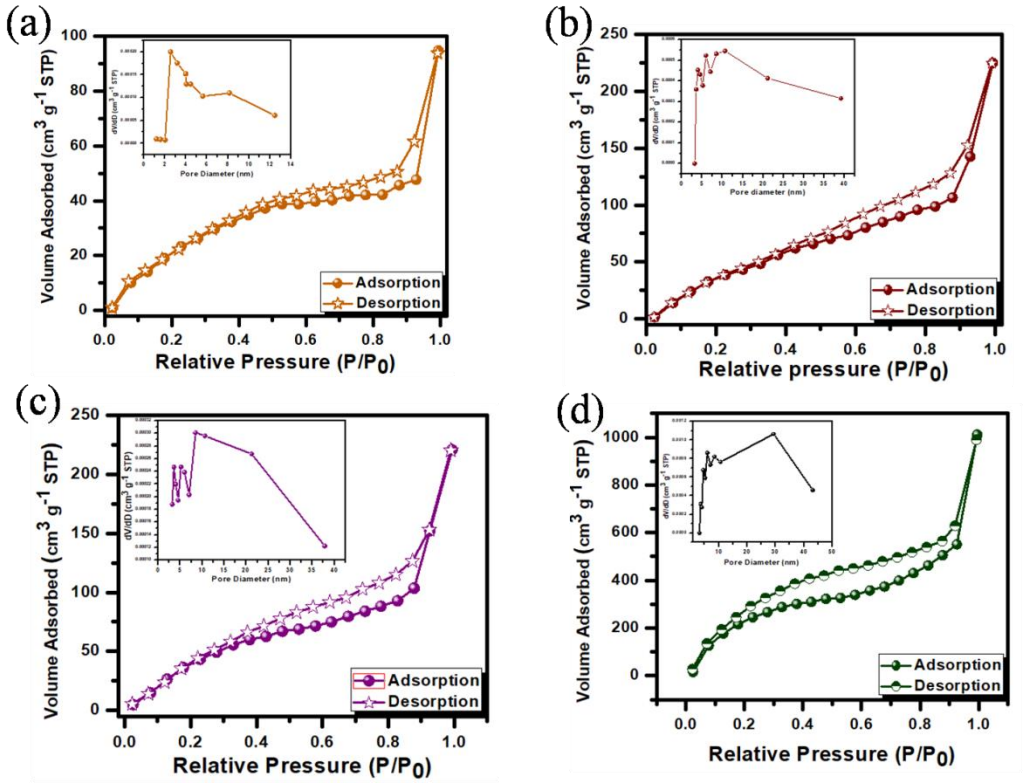

Figure 2.9: N_2 adsorption-desorption isotherms, (a) PEDOTNPs, (b) rGO/PEDOTNPs, (c) MoS_2/PEDOTNPs, and (d) MoS_2-rGO/PEDOTNPs nanocomposites.

Total pore volume has been evaluated from Barrett-Joyner-Halenda (BJH) method from desorption data and found to be 0.19 cc/g, 0.28 cc/g, 0.38 cc/g, and 0.83 cc/g for PEDOTNPs, rGO/PEDOTNPs, MoS_2/PEDOTNPs and MoS_2-rGO/PEDOTNPs nanocomposites, respectively. High specific surface area and larger pore volume of MoS_2-rGO/PEDOTNPs nanocomposites suggest efficient ion diffusion of the ternary electrode. Pore size distributions of the nanocomposites have been evaluated with BJH method and displays in the inset of corresponding isotherms. Pore distribution curve of PEDOTNPs shows sharp maxima at around 3 nm. Several concentrated aperture peaks are observed to be centered at 2 nm, 4 nm, 5.7 nm and 10.8 nm for rGO/PEDOTNPs; 1.8 nm, 3.4 nm, 5.1 nm and 8.3 nm for

MoS_2/PEDOTNPs; and 3.2 nm, 4.1 nm, 5.9 nm and 8.3 nm for MoS_2-rGO/PEDOTNPs nanocomposites. A large number of pores comfortably provide enough paths for the facile movements of the electrolyte ions [49].

Micropores with size distribution in the range of 0.7-20 nm are termed as effective micropores and K^+ electrolyte ions (hydrated, having diameter 0.6-0.7 nm) possess easy access into such pores. Sizeable mesopores can provide abundant electrochemically active sites, thus enhances the electrochemical performance for ternary nanocomposite. Ternary MoS_2-rGO/PEDOTNPs nanocomposite possesses distribution of meso and micropores which are beneficial for better penetration of electrolyte ions in the interfaces and possible electro-active sites. At the same time, mesopores provide efficient channels for reactants, electrolytes and products, enhancing catalytic efficiency and extensive charge accumulation in EDL processes [50].

3.8 Contact angle measurement: Wetting transparency of PEDOTNPs, rGO/PEDOTNPs, MoS_2/PEDOTNPs and MoS_2-rGO/PEDOTNPs nanocomposites can be understood from static contact angle measurements and enhancement of which improves the electrode-electrolyte interaction during electrochemical measurements. Contact angles of the nanocomposites have been measured using water (polar solvent) and diiodomethane (apolar solvent) and displayed in Figure 2.10. The surface energy of the testing electrodes was calculated using OWRK method [51]. The water contact angle of PEDOTNPs is 45^o and diiodomethane contact angle is 39^o. After incorporation of MoS_2 in PEDOTNPs matrix the contact angles are 81^o and 67^o for water and diiodomethane, respectively. Again, rGO/PEDOTNPs nanocomposites possess contact angles of 64^o and 60^o for water and diiodomethane, respectively. The testing liquid can penetrate the nanocomposites either by the formation of permanent dipoles or through induced dipoles between liquid and material. In 2D layered material like graphene, MoS_2, the layers are coupled with van der Waal (vdW) interaction and atoms with covalent bonding. vdW structures are not completely wetting transparent and non-polar in nature [52]. Partial wetting transparency for graphene is possible due to surface defects or π- hydrogen bonding, although it is consisted of non -polar sp^2 hybridized carbon atoms [53]. It may be the reason that the

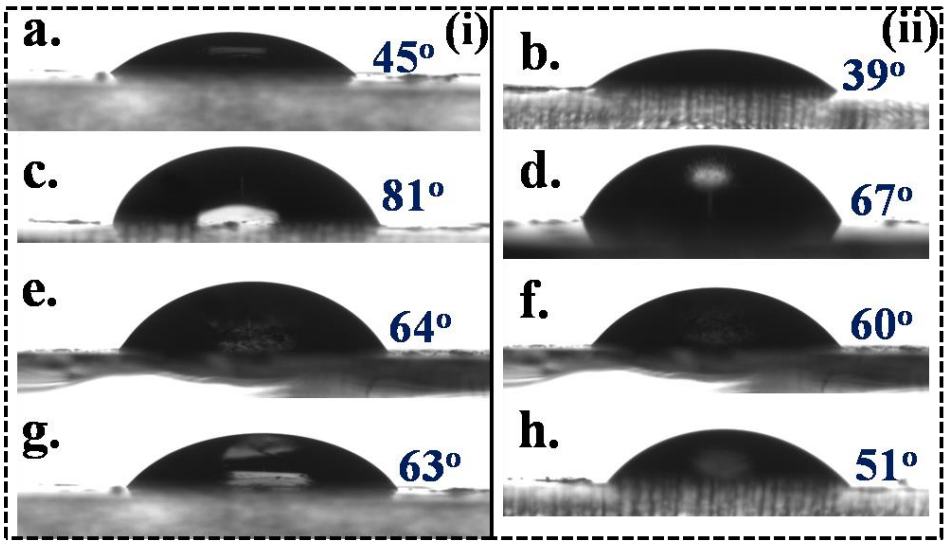

Figure 2.10: Contact angle measurements. (i) Contact angle with water of (a) PEDOTNPs, (c) MoS_2/PEDOTNPs, (e) rGO/PEDOTNPs, (g) MoS_2-rGO/PEDOTNPs nanocomposites, and (ii) with diiodomethane (b) PEDOTNPs, (d) MoS_2/PEDOTNPs, (f) rGO/PEDOTNPs, (h) MoS_2-rGO/PEDOTNPs nanocomposites.

Table 2.2: Obtained values of contact angles, polar, dispersive and total surface energies of PEDOTNPs, rGO/PEDOTNPs, MoS_2/PEDOTNPs and MoS_2-rGO/PEDOTNPs nanocomposites electrodes with water and diiodomethane.

Electrode	Water Contact angle	Diiodomethane Contact angle	Polar surface energy (γ_{sv}^{P})	Dispersive surface energy (γ_{sv}^{D})	Total surface energy (γ_{sv})
PEDOTNPs	45°	39°	18.88	40	58.88
MoS_2/PEDOTNPs	81°	67°	5.96	24.09	30.05
rGO/PEDOTNPs	64°	60°	13.35	28.57	41.92
MoS_2-rGO/PEDOTNPs	63°	51°	11.49	33.71	45.2

contact angle for rGO/PEDOTNPs nanocomposites is lower than that of MoS_2/PEDOTNPs. For ternary MoS_2-rGO/PEDOTNPs nanocomposites contact angles are found to be 63° and 51° corresponding to water and diiodomethane, respectively. Table 2.2 summarizes that the calculated dispersive surface energy is dominating over the polar surface energy and summation of both the surface energies

gives the total surface energy. The individual materials in our synthesized electrodes are rGO, MoS_2 and PEDOTNPs, where both rGO and MoS_2 are vdW individuals and non-polar in nature. Moreover, vdW individuals offer long range London dispersive force and intrinsically contribute to dispersive components of surface energy. Surface energy of the ternary nanocomposites is more which attributes the partial polar nature of rGO. The water contact angles of ternary nanocomposites have decreased suggesting improved wettability of the nanocomposites. This wettability may be attributed porous nature of MoS_2-rGO layer-by-layer structure based ternary nanocomposites.

2.4. Electrochemical characterization:

2.4.1 Electrochemical measurements of electrodes: Electrochemical performances of PEDOTNPs, rGO/PEDOTNPs, MoS_2/PEDOTNPs and MoS_2-rGO/PEDOTNPs nanocomposites have been carried out using 3 M KOH aqueous electrolyte in the potential window of -0.3 V to 0.6 V. At first, the concentrations of the KOH electrolyte were varied like 1 M, 3 M and 6 M for the optimization purpose. MoS_2-rGO/PEDOTNPs electrode showed side reactions and bubble formation in the counter electrode for concentrated 6 M KOH electrolytes. For 1 M KOH electrolyte, the current response was not as great as 3 M KOH. Therefore, we decided to proceed with 3 M KOH electrolyte for the remaining electrochemical measurements.

Cyclic voltammetry (CV) is a powerful technique to identify the charge storage processes in electrochemical measurements. CV measurements of the highly porous PEDOTNPs, rGO/PEDOTNPs, MoS_2/PEDOTNPs and MoS_2-rGO/PEDOTNPs electrodes are shown in Figure 2.11 at the scan rate of 40 mVs^{-1}. Bare Ni foam (NF) adds on negligible contribution to the overall capacity of the electrodes, as observed from CV measurements (Figure 2.11 a). A pair of redox peaks has been observed for the CV curves of PEDOTNPs attributed to the faradic reaction of K^+ ions to/from the redox sites of the polymer. Pristine PEDOTNPs electrode exhibits a weak oxidation peak at 0.46 V and reduction peak at ~ 0 V which are corroborating with the CV results of Mao et al. [54]. Jang et al. [55] also performed CV measurements for PEDOT nanoparticles, PEDOT nanocapsules, and PEDOT mesocellular foams and observed a pair of redox peaks around 0.47 V and 0.35 V for PEDOT nanoparticles only. The capacitive response has been increased for rGO/PEDOTNPs electrode than that of PEDOTNPs after incorporation of rGO in polymer matrix which has further

enhanced for binary MoS_2/PEDOTNPs electrode (Figure 2.11 a). Ternary MoS_2-rGO/PEDOTNPs electrode possesses much larger integral area under the CV curves, which suggests the improved storage ability of the electrode when compared with PEDOTNPs, rGO/PEDOTNPs, MoS_2/PEDOTNPs as specific capacitance is directly proportional to the CV area encloses (C_{sp} α ∫IdV). The reduction and oxidation peaks are appearing around 0.4 V and 0.13 V for MoS_2-rGO/PEDOTNPs electrode, respectively. MoS_2 provide pseudocapacitance in alkaline media according to Liu et al. [56], whereas rGO is the EDLC component. In ternary electrode, energy storage processes may involve the transition between redox states of PEDOT i.e. benzoid and quinoid structures and the possible redox reactions for MoS_2 are expressed below [56, 57].

$MoS_2 + K^+ \leftrightarrow$ MoS-SK (faradic component)

$(MoS_2)_{surface} + K^+ + e^- \leftrightarrow (MoS^- - SK^+)_{surface}$ (non-faradic component)

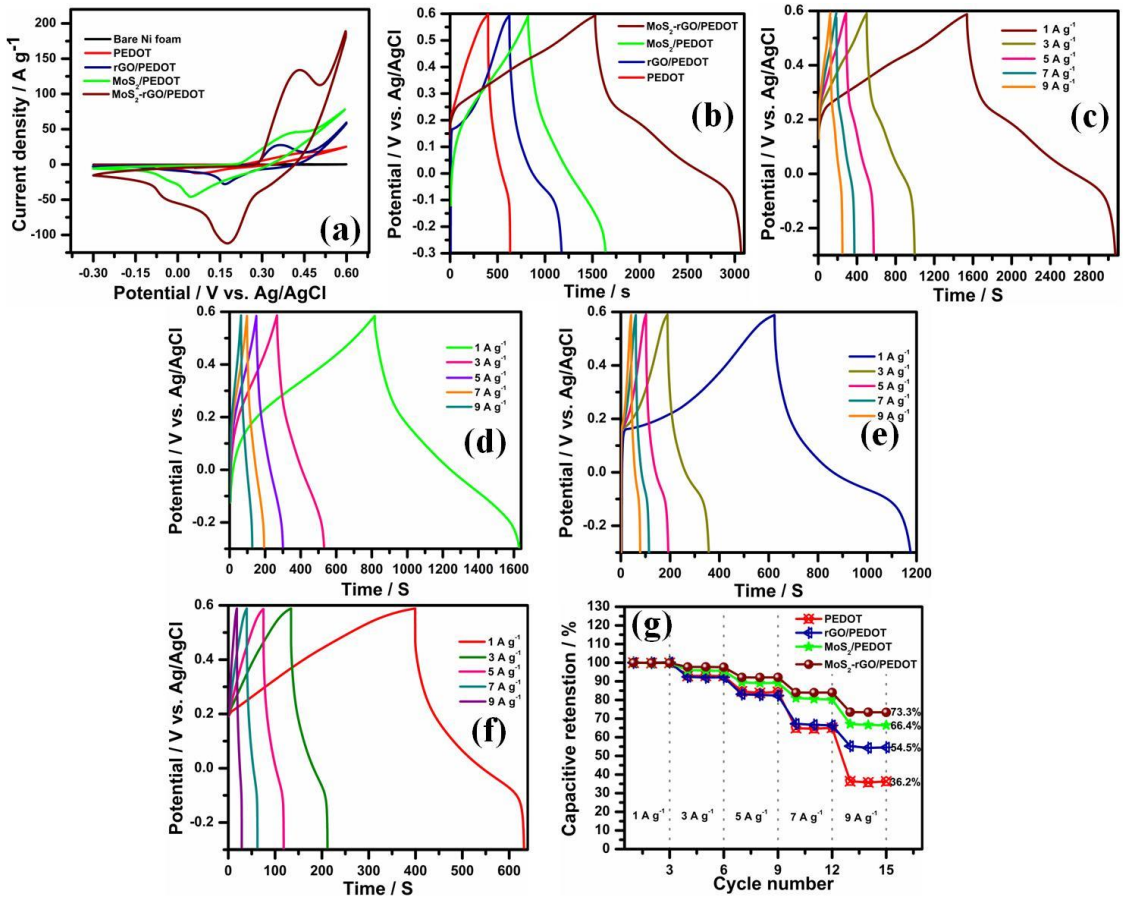

Figure 2.11: (a) Cyclic voltammetry (CV) and (b) Galvanostatic charge-discharge (GCD) measurements of PEDOTNPs, rGO/PEDOTNPs, MoS_2/PEDOTNPs and MoS_2-rGO/PEDOTNPs nanocomposites; GCD at different current densities for (c)

MoS_2-rGO/PEDOTNPs electrodes, (d) MoS_2/PEDOTNPs electrodes, (e) rGO/PEDOTNPs electrodes, (f) PEDOTNPs electrodes; (g) rate capability plot.

MoS_2 helps in the dispersion of polymer matrix in nanocomposites and rGO acts as a highly conductive network providing easy ion motion between electrode and electrolyte in the ternary nanocomposites. Moreover, loosely arranged layer-by-layer structure of MoS_2-rGO supplies additional electro-active sites in the hetero-interfaces and higher bending modulus of MoS_2 prevents the agglomeration of rGO sheets in MoS_2-rGO layer-by-layer structures (observed from TEM images) [58]. Therefore, the highly efficient charge storage behaviour of ternary MoS_2-rGO/PEDOTNPs electrode is attributed to the synergetic effects of MoS_2, rGO and PEDOTNPs, porous structures, improved electrode/ electrolyte interactions (contact angle measurements), and larger specific surface area (BET results).

GCD measurements of PEDOTNPs, rGO/PEDOTNPs, MoS_2/PEDOTNPs and MoS_2-rGO/PEDOTNPs electrodes have been carried out at the current density of 1 Ag^{-1} in 3 M KOH electrolyte for the potential window of -0.3 V to 0.6 V and the curves are shown in Figure 2.11 b. Both the charging and discharging pattern of PEDOTNPs electrode is nonlinear with a specific capacitance of 187.4 Fg^{-1} attributed to the pseudocapacitive nature of PEDOTNPs. rGO/PEDOTNPs electrode with specific capacitance of 405 Fg^{-1} possesses quasi-linear characteristics due to the EDLC contribution from rGO and pseudocapacitance from PEDOTNPs. MoS_2-PEDOTNPs electrode offers specific capacitance of 615.5 Fg^{-1} with two plateaus in the discharge curves attributed to the faradic reactions in the Mo redox sites and PEDOTNPs. The ternary MoS_2-rGO/PEDOTNPs electrode with highest discharge duration delivers 1143.7 Fg^{-1} of specific capacitance (1 Ag^{-1} current density).

GCD measurements of the electrodes also have been performed at 3, 5, 7 and 9 Ag^{-1} of current densities and shown in Figure 2.11 (c-f). Specific capacitances of the electrodes have been calculated for different currents and the rate capability plot is displayed in Figure 2.11 g for three consecutive cycles at the same current density. PEDOTNPs, rGO/PEDOTNPs and MoS_2/PEDOTNPs electrodes exhibit 36.2%, 54.5% and 66.4% of rate capability at the current density of 9 Ag^{-1}. The ternary MoS_2-rGO/PEDOTNPs electrode possesses 1117 Fg^{-1} (97.6%), 1053 Fg^{-1} (92%), 960 Fg^{-1} (83.9%) and 840 Fg^{-1} (73.3%) of specific capacitance at the current density of 3, 5, 7 and 9 Ag^{-1}, respectively. It is observed that, specific capacitance decreases with

increasing current densities as the slow processes are not possible in less time [59]. rGO/PEDOTNPs electrode possesses better capacitive retention than that of PEDOTNPs and MoS_2-PEDOTNPs which may be attribute to conducting rGO network. The probable explanations for high-rate capability of MoS_2-rGO/PEDOTNPs electrode are: MoS_2-rGO layer-by-layer structures contribute larger surface area by minimizing agglomeration of the nanosheets, more number of electro-active sites and interfaces for easy access of the electrolyte ions for the ternary electrode.

The kinetic behaviour of the supercapacitor electrodes has been further studied with CV measurements by deconvoluating the contributions from both the charge storage processes: (i) diffusion controlled faradic process and (ii) non-diffusive capacitive process using the following model [60]:

$$i(V) = a\vartheta^b \tag{2.8}$$

where, $i(V)\ and\ \vartheta$ are corresponding to the response current at a particular voltage and scan rate, respectively. Slop of $\log i\ vs.\ \log \vartheta$ gives the "b" value. If the "b" value is 0.5 then charge storage at electrode purely dominates by diffusion-controlled process. The "b" value 1 suggests the presence of pure capacitive controlled

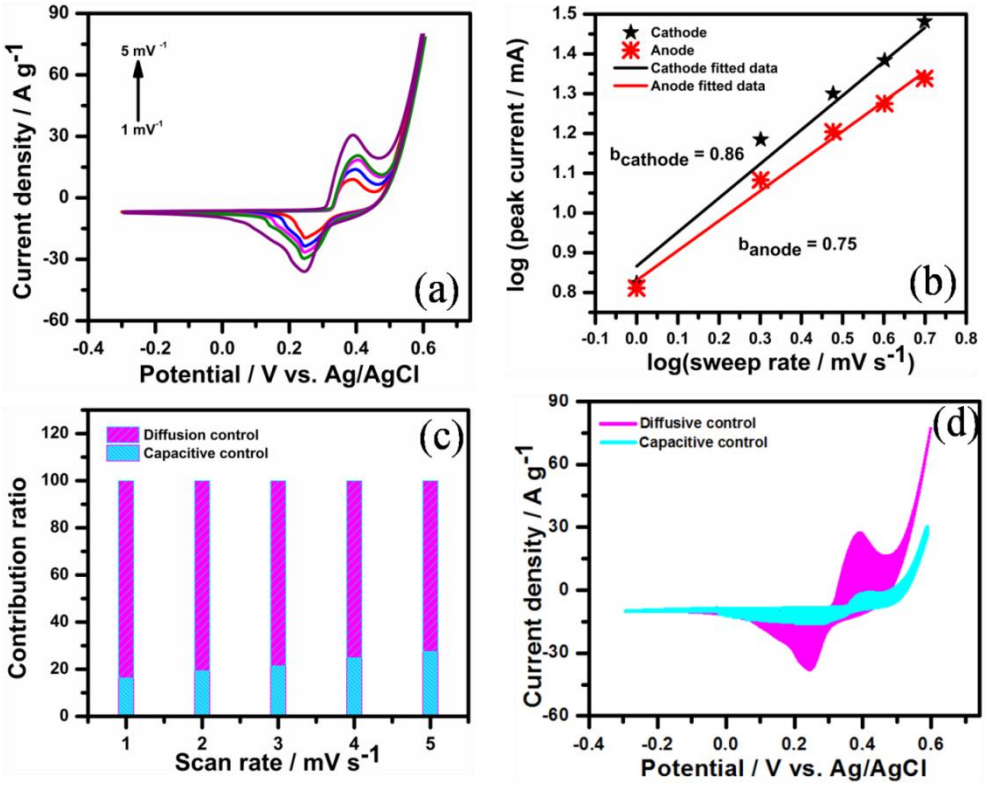

Figure 2.12: (a) CV measurements of MoS_2-rGO/PEDOTNP electrode at scan rates of 1 mVs^{-1} to 5 mVs^{-1}, (b) plot of log (peak current) vs. log (sweep rate) for 1 mVs^{-1}

to 5 mVs^{-1}, (c) relative contribution of diffusive and capacitive controlled charge storage processes at different scan rates for 1 mVs^{-1} to 5 mVs^{-1} and (d) Capacitive-controlled and diffusion-controlled charge storage processes for 1 mVs^{-1} to 5 mVs^{-1}.

processes. When "b" value is 0.5, then the current is proportional to square root of the scan rates suggesting complete diffusion-controlled contribution and obeys randles-sevcik equation [60, 61]. Complete capacitive response is observed for "b" value of 1. Dunn et al. [60] reported that "b" value of 0.55 attributed to the intercalation of electrolyte ions and "b" value in the range of 0.8 to 1 indicated predominantly capacitive behavior for current. For that purpose, CV measurements of the ternary MoS_2-rGO/PEDOTNPs electrodes have been taken at lower scan rates of 1 mVs^{-1} to 5 mVs^{-1} (Figure 2.12 a) to get a clear information about the charge storage processes and log (peak current) vs. log ϑ has been plotted (Figure 2.12 b). The area of the CV curves increases with increasing scan rates and preserves the overall CV pattern at higher sweeping rate indicating the presence of electrochemical reversibility of the ternary electrode. The fitted "b" values for the scan range of 1 mVs^{-1} to 5 mVs^{-1} are 0.86 and 0.75 for the cathodic and anodic peaks, respectively. Thus, contribution of both diffusion and surface-controlled charge storage mechanisms is possible in ternary MoS_2-rGO/PEDOTNPs electrode. Further the deconvoluation of capacitive and diffusion contributions to the total charge storage have been carried out using the following equation:

$$i(V) = k_1\vartheta + k_2\vartheta^{\frac{1}{2}} \tag{2.9}$$

where, $k_1\vartheta$ and $k_2\vartheta^{\frac{1}{2}}$ represent the capacitive contribution and diffusion contribution, respectively, k_1 and k_2 are constants, and ϑ is the scan rate at which $i(V)$ current is measured. The fragment of current contribution at a specific voltage can be established by calculating k_1 and k_2 from the above equation. Swift ion diffusion considerably enhances the charging / discharging ability of the electrode material at higher current densities [62, 63]. Figure 2.12 c shows the deconvoluated contribution of both the processes at different scan rates of 1 mVs^{-1} to 5 mVs^{-1}. The surface capacitive contribution is obtained to be 16.27% and 27.5% at scan rate of 1 mVs^{-1} and 5 mVs^{-1} to the overall storage process of ternary MoS_2-rGO/PEDOTNPs nanocomposite respectively (Figure 2.12 c). Deconvoluated CV profiles for ternary MoS_2-rGO/PEDOTNPs electrode at the scan rate of 5 mVs^{-1} is displayed in Figure

2.12 d. Observed cyan colored region (Figure 2.12 d) is corresponding to capacitive controlled contribution at scan rate of 5 mVs^{-1} which is 27.5% of the overall contribution. Tao et al. [62] deconvoluaed the charge storage processes for $Li_2Ni_2(MoO_4)_3$ in 2 M LiOH solution using the equation 2.9 and obtained 50.7% of diffusion-controlled contribution at scan rate of 5 mVs^{-1}. Du et al. [63] reported sodium naphthalene-2, 6-bis(carbothioate) based electrodes for lithium battery and found 43% of diffusion contribution at scan rate of 1 mVs^{-1}. Wang et al. [64] and Gao et al. [65] also deconvoluated the storage processes for nitrogen-doped TiO_2-C composite nanofibers and commercial expanded graphite based electrodes for the application of sodium-ion batteries and aluminum ion battery, respectively.

The cycling stability of PEDOTNPs, rGO/PEDOTNPs, MoS_2/PEDOTNPs and MoS_2-rGO/PEDOTNPs electrodes have been carried out in 3 M KOH electrolyte for 3000 repeated GCD cycles (20 Ag^{-1}) (Figure 2.13 a). Ternary MoS_2-rGO/PEDOTNPs electrodes exhibit 97.7% of cycling stability after repeated 3000 GCD cycles. The porous arrangement of ternary nanocomposites can accommodate the volumetric

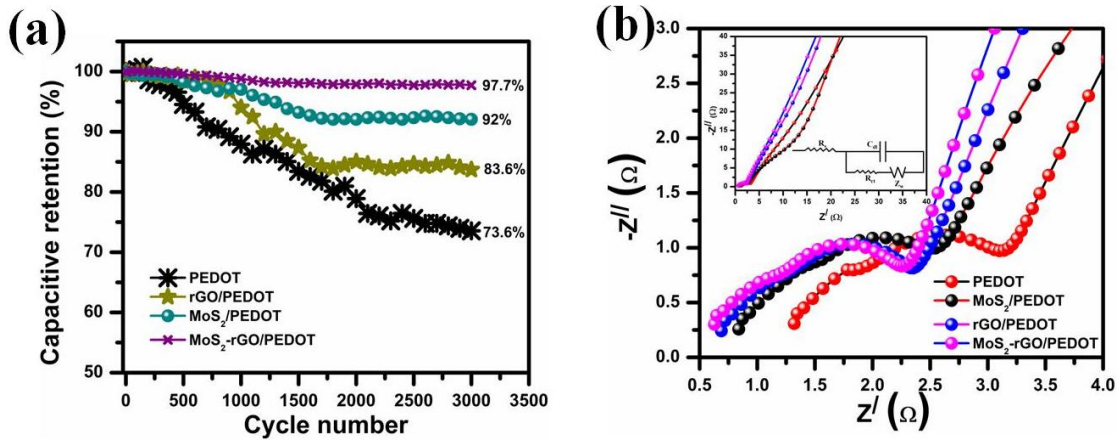

Figure 2.13: (a) Cycling stability up to 3000 cycles and (b) electrochemical impedance spectroscopy (EIS) measurements of PEDOTNPs, rGO/PEDOTNPs, MoS_2/PEDOTNPs and MoS_2-rGO/PEDOTNPs electrodes.

swelling of PEDOTNPs up to some extent and hence maintains the mechanical strength of the electrodes, leading to enhance cycling stability. PEDOTNPs, rGO/PEDOTNPs, MoS_2/PEDOTNPs electrodes possess 73.6%, 83.6% and 92% of capacitive retention after 3000 repeated GCD cycles, respectively. The poor stability of PEDOTNPs electrode is attributed to the shrinkage and swelling in the polymer backbone leading to the overall degradation of the electrode. Enhanced stability

performance of rGO/PEDOTNPs and MoS_2/PEDOTNPs nanocomposites could be observed from the better dispersion of the conducting polymer in the binary nanocomposites and synergistic effects.

Electrochemical impedance spectroscopy (EIS) measurements of PEDOTNPs, rGO/PEDOTNPs, MoS_2/PEDOTNPs and MoS_2-rGO/PEDOTNPs electrodes in the frequency range of 10^7 to 0.001 Hz are displayed in Figure 2.13 b, inset shows the equivalent circuit. EIS spectra of all the electrodes exhibit distinct suppressed semi-circular feature. The first X-axis intercept of the semi-circular arc at the high frequency is equivalent series resistance (R_s) which is the measure of ionic resistance of electrolyte with electrode's intrinsic resistance. The diameter of the semi-circle is charge transfer resistance (R_{ct}) at electrode/electrolyte interfaces. 1.32 Ω, 0.84 Ω, 0.7 Ω, 0.62 Ω are the values of R_s and 1.83 Ω, 1.71 Ω, 1.66 Ω, 1.63 Ω are observed R_{ct} values for PEDOTNPs, rGO/PEDOTNPs, MoS_2/PEDOTNPs and MoS_2-rGO/PEDOTNPs nanocomposites, respectively. From PEDOTNPs to the ternary MoS_2-rGO/PEDOTNPs electrodes, R_s continuously decreases due to the incorporation of MoS_2 and rGO in binary nanocomposites where MoS_2 helps in better dispersion of the polymer matrix and highly conductive rGO reduces the electrode intrinsic resistance. Warburg impedance (W_o), the linear portion after the semicircle

Table 2.3: Values of equivalent series resistance (R_s), charge transfer resistance (R_{ct}) and knee frequency (f_{knee}) from EIS measurements.

Electrode	Equivalent series resistance (R_s)	Charge transfer resistance (R_{ct})	Knee frequency (f_{knee})
PEDOTNPs	1.32 Ω	1.83 Ω	25.119 Hz
MoS_2/PEDOTNPs	0.7 Ω	1.66 Ω	31.62 Hz
rGO/PEDOTNPs	0.84 Ω	1.71 Ω	25.119 Hz
MoS_2-rGO/PEDOTNPs	0.62 Ω	1.63 Ω	39.81 Hz

of Nyquist plot at 45^o slop in middle frequency region appears due to frequency dependent diffusion limited ion transportation in the electrolyte. Smaller Warburg region of the ternary MoS_2-rGO/PEDOTNPs electrode indicates shorter diffusion paths of the electrolyte ions in MoS_2-rGO layer-by-layer structures, as well as the layered structure assists the motion of ions, resulting in higher knee frequency (f_{knee}).

f_{knee} is the parameter at which the system comes out from resistance regimes and capacitive process dominates. The values of R_s, R_{ct} and f_{knee} are displayed in Table 2.3. The steep rise of Nyquist plots after the knee frequency for all the electrodes is suggesting capacitive behavior. The ease of ion diffusion for ternary MoS_2-rGO/PEDOTNPs electrode is due to the higher surface area, better pore structures, connectivity and more number of interfaces.

2.4.2 Electrochemical measurements of symmetric supercapacitor: Till now, electrochemical properties of PEDOTNPs, rGO/PEDOTNPs, MoS_2/PEDOTNPs and

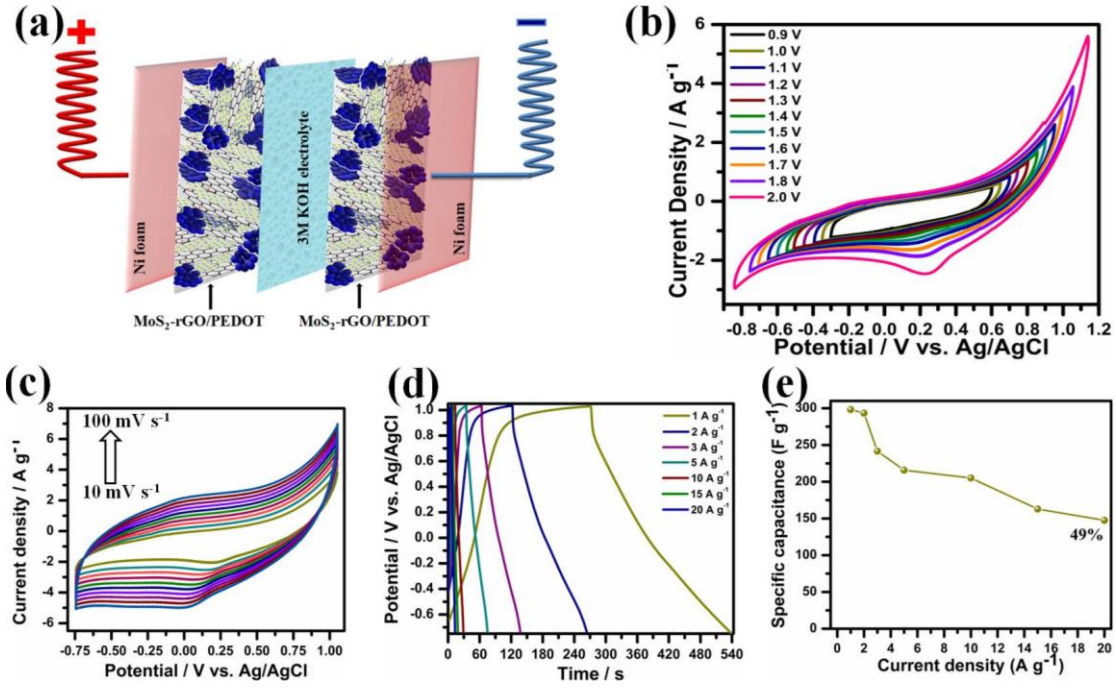

Figure 2.14: (a) Schematic representation of MoS_2-rGO/PEDOTNPs // MoS_2-rGO/PEDOTNPs symmetric supercapacitor, (b) CV for potential window optimization, (c) CV at different scan rates, (d) GCD at different current densities, and (e) rate capability plot of MoS_2-rGO/PEDOTNPs // MoS_2-rGO/PEDOTNPs symmetric supercapacitor.

MoS_2-rGO/PEDOTNPs electrodes have been discussed. Among them, ternary MoS_2-rGO/PEDOTNPs electrode has been selected to evaluate electrode real time application due to its remarkable electrochemical properties than that of the others. Symmetric supercapacitor (SSC) was constructed by conforming MoS_2-rGO/PEDOTNPs as both positive and negative electrodes and properties were investigated using 3 M KOH electrolyte. The scheme of SSC assembly has been

depicted in Figure 2.14 a. The optimum potential window of the symmetric supercapacitor was investigated from a set of CV measurements at scan rate of 10 mVs^{-1} (Figure 2.14 b) by equally increasing the potential on both the sides of capacitive potential range (-0.3 V to 0.6 V vs. Ag/AgCl) of the ternary electrode. It is observed that the operating potential window of the SSC can be extended as high as 1.8 V which is also the combined potential range of two ternary electrodes (Figure 2.14 b). Beyond 1.8 V, large current in CV pattern indicates electrolysis of aqueous electrolyte. Figure 2.14 (c) depicts the CV behavior of as fabricated MoS_2-rGO/PEDOTNPs // MoS_2-rGO/PEDOTNPs symmetric supercapacitor at different scan rates from 10 mVs^{-1} to 100 mVs^{-1} for the optimized 1.8 V potential limit. The symmetric supercapacitor exhibits quasi-rectangular shaped CV characteristics attributed to the presence of both pseudocapacitance and EDLC mechanisms. The shape of CV pattern is almost identical (Figure 2.14 c) at high scan rate of 100 mVs^{-1} also and CV area increases with increasing scan rate, suggesting good capacitive behaviour of the symmetric supercapacitor in the optimized potential range. GCD measurements of the symmetric supercapacitor were carried out for the current densities of 1 Ag^{-1} to 20 Ag^{-1} in the potential window of -0.75 V to 1.05 V (Figure 2.14 d). GCD curves of symmetric supercapacitor exhibit non-linear geometry due to the contribution of both EDLC and pseudocapacitance which corroborates the CV results. Specific capacitance for the SSC was calculated to be 298.25 Fg^{-1} at 1 Ag^{-1} of current density and 147.5 Fg^{-1} at 20 Ag^{-1} of current density possessing 49.45% of rate capability. The rate capability plot for the fabricated symmetric supercapacitor is depicted in Figure 2.14 (e). It is obvious that at high current density (20 Ag^{-1}), charging/discharging processes are very quick and for that slow diffusion processes may suffer time constraint [59]. However, shapes of CV and GCD of MoS_2-rGO/PEDOTNPs // MoS_2-rGO/PEDOTNPs symmetric supercapacitor suggest the contribution of both EDLC and pseudocapacitance at slow rates. Non-diffusive charge storage mechanism mainly contributes to overall capacity at high current rates resulting only 49.45% of capacitive retention. Rate performances of some of already reported symmetric supercapacitors have been compared in table no. 2.4 where MoS_2/ RGO@PANI // MoS_2/RGO@PANI exhibit rate performance of 40% at current density of 10 Ag^{-1} [66].

Cycling stability, one of the most important parameters of the fabricated symmetric supercapacitor in practical applications, was carried out for 10,000

repeated GCD cycles at 20 Ag^{-1} of current density. The specific capacitance retention vs. cycle numbers is shown in Figure 2.15 (a). It is observed that the symmetric supercapacitor retains specific capacitance of 151.1 Fg^{-1} (102.2%), 149.3 Fg^{-1} (101.12%), 146.57 Fg^{-1} (99.36%), 143.19 Fg^{-1} (97.07%), 142 Fg^{-1} (96.27%) and 137.43 Fg^{-1} (93.17%) after 1000, 2000, 3000, 4000, 5000 and 10,000 repeated GCD cycles, respectively.

Table 2.4: Comparison of calculated parameters of some reported symmetric supercapacitors with the fabricated MoS_2-rGO/PEDOTNPs // MoS_2-rGO/PEDOTNPs symmetric supercapacitor.

Sl. no	Electrode material	Specific capacitance (Current density)	Rate capability (Current density)	Cycling stability (Cycle number)	Specific Energy / Wh kg^{-1}	Specific Power / W kg^{-1}	Ref
1	MoS_2/ RGO@PANI // MoS_2/ RGO@PANI	160 F g^{-1} (1 Ag^{-1})	40% (10 A g^{-1})	-	22.3	5080	66
2	MoS_2 nanodots // MoS_2 nanodots	122 Fg^{-1} (1 Ag^{-1})	39.3% (10 Ag^{-1})	86% (1k)	22	1300	67
3	MoS_2 // MoS_2	244 Fg^{-1} (1 Ag^{-1})	-	92% (9k)	12.2	600	68
4	PEDOT // PEDOT	198 Fg^{-1} (0.5 Ag^{-1})	70% (100 Ag^{-1})	86% (12k)	4.4	200	69
5	Activated carbon (AC) / rGO // AC / rGO	95.2 Fg^{-1} (0.5 Ag^{-1})	69.7% (20 Ag^{-1})	97% (8k)	11.9	469.24	70
6	NiS/ rGO // NiS/ rGO	14.2 Fg^{-1} (0.1 Ag^{-1})	28.73% (1 Ag^{-1})	-	7.1	1836	71
7	rGO/ Mn_3O_4 //	243 Fg^{-1} (0.5 Ag^{-1})	41.15% (5 Ag^{-1})	82.3% (1k)	27.92	277.78	72

	rGO/ Mn_3O_4						
8	CNT/ PEDOT // CNT/ PEDOT	51 Fg^{-1} (0.5 Ag^{-1})	-	95% (3k)	12.6	1200	73
9	Cl^- - PEDOT /graphite // Cl^- - PEDOT /graphite	178 Fg^{-1} (0.5 Ag^{-1})	41% (100 Ag^{-1})	86% (10k)	6.19	250	74
10	MoS_2-rGO/PEDOT // MoS_2-rGO/PEDOT	298 Fg^{-1} (1 Ag^{-1})	49% (20 Ag^{-1})	93% (10k)	33.56	450	This work

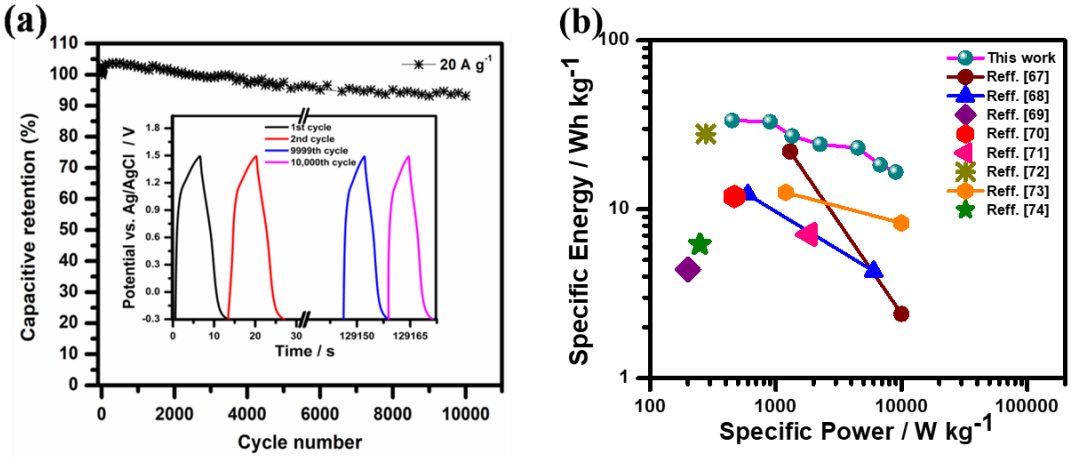

Figure 2.15: (a) Cycling stability plot of MoS_2-rGO/PEDOTNPs // MoS_2-rGO/PEDOTNPs symmetric supercapacitor up to 10,000 cycles (inset shows the first and last two cycles), and (b) Ragone plot of MoS_2-rGO/PEDOTNPs // MoS_2-rGO/PEDOTNPs symmetric supercapacitor.

Ragone plot has been explored by calculating specific energy and power of the as fabricated symmetric supercapacitor as a function of current densities (Figure 2.15 b). MoS_2-rGO/PEDOTNPs // MoS_2-rGO/PEDOTNPs symmetric supercapacitor delivers specific energy of 33.56 $Whkg^{-1}$ based on the total mass when specific power is 450.03 Wkg^{-1} at 1 Ag^{-1} of current density. The symmetric supercapacitor retains

specific energy of 16.59 $Whkg^{-1}$ with high specific power of 8997.42 Wkg^{-1} at 20 Ag^{-1} of current density. These values are superior to many PEDOTNPs, MoS_2 and rGO based symmetric supercapacitors. Table 2.4 compares the calculated parameters of some of already reported symmetric supercapacitors with fabricated MoS_2-rGO/PEDOTNPs // MoS_2-rGO/PEDOTNPs [66-74]. Ternary MoS_2-rGO and PEDOTNPs nanocomposite based symmetric supercapacitor with improved electrode/ electrolyte interaction, elevated surface area is a suitable nominee for supercapacitor applications that performs outstanding at high current density regime.

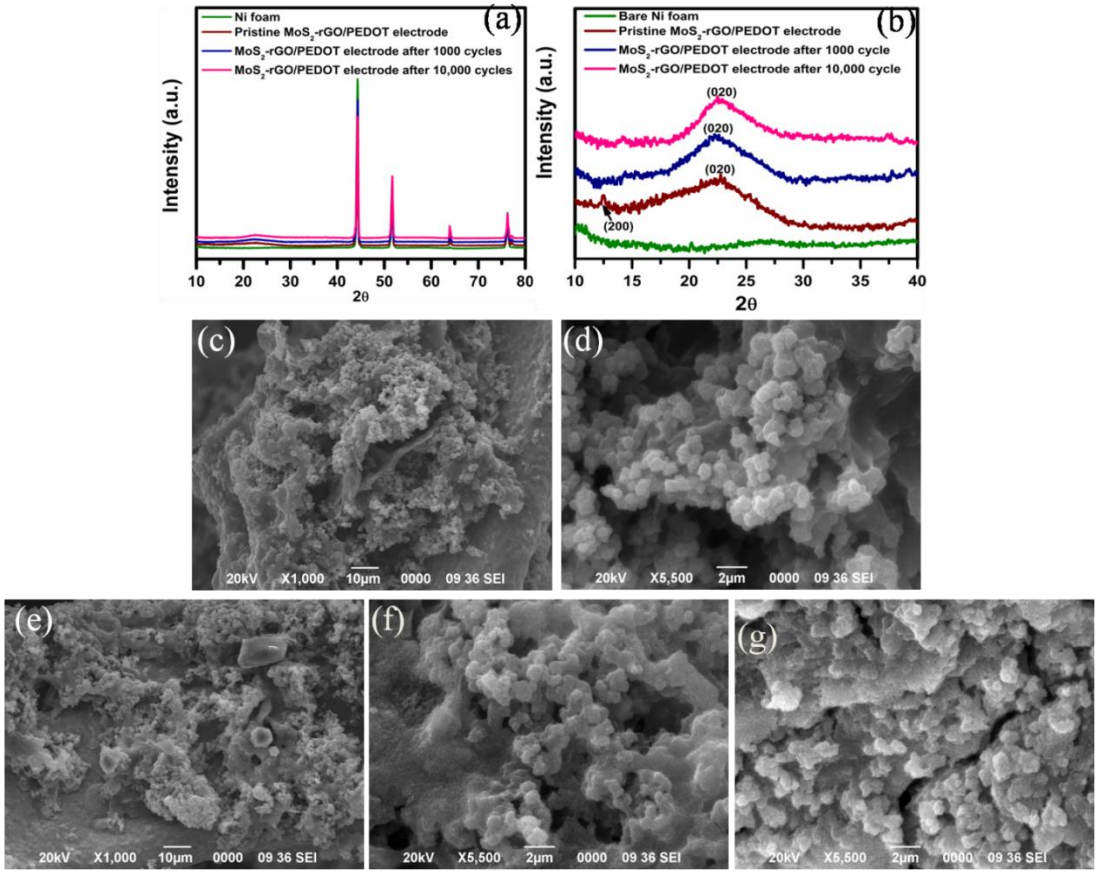

Figure 2.16: (a, b) *Ex-situ* XRD pattern of bare Ni foam, pristine MoS_2-rGO/PEDOTNPs electrode, MoS_2-rGO/PEDOTNPs electrode after 1000 and 10,000 GCD cycles; SEM micrographs of (c), (d) pristine MoS_2-rGO/PEDOTNPs electrode at resolution of 10 μm and 2 μm, respectively, (e, f, g) MoS_2-rGO/PEDOTNPs electrode after 10,000 GCD cycles at resolution of 10 μm and 2 μm, respectively.

In order to explore the phase and morphology changes of MoS_2-rGO/PEDOTNPs electrode after repeated cycling, *ex-situ* XRD and SEM have been performed for the ternary electrode before and after the stability test (Figure 2.16).

Ex-situ XRD profile of bare Ni foam, pristine MoS_2-rGO/PEDOTNPs electrode, MoS_2-rGO/PEDOTNPs electrode after 1000 cycles and MoS_2-rGO/PEDOTNPs electrode after 10,000 cycles are depicted in Figure 2.16 a. The characteristic peaks of active material i.e. ternary MoS_2-rGO/PEDOTNPs is appearing in the range of $2\theta = 10^o - 40^o$ and for that, XRD pattern within that 2θ range is concentrated to understand the effect of repeated GCD cycling on crystallography of the electrode and depicts in Figure 2.16 b. *Ex-situ* XRD patterns (Figure 2.16 b) of the ternary electrode don't indicate distinguishable crystallographic changes except the disappearance of polymer peak corresponding to (200) plane around $2\theta = 12.5^o$. Disappearance of the XRD peak suggests the loss of 2D stacking in PEDOTNPs chain after repeated GCD cycles [32].

SEM images of pristine MoS_2-rGO/PEDOTNPs electrode are depicted in Figure 2.16 (c) and (d) at different magnifications. At some portions MoS_2-rGO layer-by-layer structure is noticed below PEDOTNPs for the ternary electrode. Pseudocapacitive materials offer poor cycling stability attributed to swelling and shrinkage during galvanostatic cycling [9]. This causes mechanical degradation in the electrode material, as a result of which capacitive performance of the electrode degrades. Swelling and shrinkage have been observed for PEDOTNPs (Figure 2.16 f) of the ternary MoS_2-rGO/PEDOTNPs electrode after repeated galvanostatic cycling and as a result of which at some portions nanosheets have been observed without the polymer covering (Figure 2.16 e, f). But, layered and mesoporous structure of ternary MoS_2-rGO/PEDOTNPs electrode can accommodate the volumetric changes of the polymer nanoparticles (Figure 2.16 g), preventing the electrode from mechanical degradation during repeated GCD cycles. Thus, ternary MoS_2-rGO/PEDOTNPs electrode exhibits remarkable stability in practical applications.

2.5 Conclusion

In summary, MoS_2-rGO layer-by-layer structures were synthesized by one-step self-assembly method. Ternary MoS_2-rGO/PEDOTNPs nanocomposites were synthesized with PEDOTNPs and MoS_2-rGO layer-by-layer structures exploiting one-step hydrothermal reduction process. Ternary MoS_2-rGO/PEDOTNPs nanocomposite shows no agglomeration as observed from TEM images. The nanocomposite possesses high specific surface area (528 m^2g^{-1}) and larger pore volume (0.83 ccg^{-1})

which provide efficient ion diffusion pathways through the ternary nanocomposite. Wetting transparency of ternary electrodes has been improved and it is attributed to the partial polar nature of rGO and hydrophilic PEDOTNPs. Ternary MoS_2-rGO/PEDOTNPs electrode exhibits highest specific capacitance of 1143.7 Fg^{-1} at 1 Ag^{-1} of current density and rate capability of 73.3% at 9 Ag^{-1} of current density. Ternary electrode exhibits cycling stability of 97.7% after repeated 3000 galvanostatic cycles at 20 Ag^{-1} of current density. MoS_2-rGO/PEDOTNPs // MoS_2-rGO/PEDOTNPs symmetric supercapacitor was assembled to investigate the practical application of the ternary electrode. The symmetric supercapacitor delivers specific capacitance of 289.25 Fg^{-1} at 1 Ag^{-1} of current density and rate capability of 49% at 20 Ag^{-1} of current density. The supercapacitor exhibits excellent cycling stability of 93.17% after 10,000 galvanostatic cycles at 20 Ag^{-1} of current density. Moreover, specific energy of 33.56 $Whkg^{-1}$ could be achieved with a specific power of 450.03 Wkg^{-1} by the symmetric supercapacitor based on the total mass at 1 Ag^{-1} of current density. These values are respectively 16.59 $Whkg^{-1}$ and 8997.42 Wkg^{-1} at 20 Ag^{-1} of current density. This work explains a facile approach for preparing ternary nanocomposite of MoS_2, rGO and PEDOTNPs which demonstrates good electrochemical stability for supercapacitor.

2.6 References

[1] Jiang, L., Zhang, S., Kulinich, S. A., Song, X., Zhu, J., Wang, X., and Zeng, H. Optimizing hybridization of 1T and 2H phases in MoS_2 monolayers to improve capacitances of supercapacitors. *Materials Research Letters*, 3(4): 177-183, (2015).

[2] Gopalakrishnan, K., Sultan, S., Govindaraj, A., and Rao, C. N. R. Supercapacitors based on composites of PANI with nanosheets of nitrogen-doped RGO, BC1. 5N, MoS_2 and WS_2. *Nano Energy*, 12: 52-58, 2015.

[3] Wang, K., Dong, X., Zhao, C., Qian, X., and Xu, Y. Facile synthesis of Cu2O/CuO/RGO nanocomposite and its superior cyclability in supercapacitor. *Electrochimica Acta*, *152*: 433-442, 2015.

[4] Bhat, U., and Meti, S. Graphene-Based ZnO Nanocomposites for Supercapacitor Applications. *Graphene as Energy Storage Material for Supercapacitors*, 64: 181, 2020.

[5] Lu, X., Zeng, Y., Yu, M., Zhai, T., Liang, C., Xie, S., Balogun, M. S. and Tong, Y. Oxygen-deficient hematite nanorods as high performance and novel negative electrodes for flexible asymmetric supercapacitors. *Advanced materials*, 26(19): 3148-3155, 2014.

[6] Yu, M., Zhang, Y., Zeng, Y., Balogun, M.S., Mai, K., Zhang, Z., Lu, X., and Tong, Y. Water surface assisted synthesis of large scale carbon nanotube film for high performance and stretchable supercapacitors. *Advanced Materials*, 26(27): 4724-4729, 2014.

[7] Hussain, I., Mohapatra, D., Dhakal, G., Lamiel, C., Mohamed, S. G., Sayed, M. S., Lee, Y.R., Lee, J., Lee, M., and Shim, J. J. Growth of 2D nanoflakes from 1D long leaf arrays: Electrochemical influence of copper and nickel co-substituted cobalt oxide. *Journal of Energy Storage*, 32: 101871, 2020.

[8] Maity, C. K., Goswami, N., Verma, K., Sahoo, S., and Nayak, G. C. A facile synthesis of boron nitride supported zinc cobalt sulfide nano hybrid as high-performance pseudocapacitive electrode material for asymmetric supercapacitors. *Journal of Energy Storage*, 32: 101993, 2020.

[9] Sarmah, D., and Kumar, A. Layer-by-layer self-assembly of ternary MoS_2-rGO@ PPyNTs nanocomposites for high performance supercapacitor electrode. *Synthetic Metals*, 243: 75-89, 2018.

[10] Liu, Y., Murtaza, I., Shujia, A., and Meng, H. Interfacial modification for heightening the interaction between PEDOT and substrate towards enhanced flexible solid supercapacitor performance. *Chemical Engineering Journal*, 379: 122326, 2020.

[11] Balogun, M. S., Zeng, Y., Qiu, W., Luo, Y., Onasanya, A., Olaniyi, T. K., and Tong, Y. Three-dimensional nickel nitride (Ni_3N) nanosheets: free standing and flexible electrodes for lithium ion batteries and supercapacitors. *Journal of Materials Chemistry A*, 4(25): 9844-9849, 2016.

[12] Su, H., Xiong, T., Tan, Q., Yang, F., Appadurai, P., Afuwape, A. A., Balogun, M.S., Huang, Y. and Guo, K. Asymmetric Pseudocapacitors Based on Interfacial Engineering of Vanadium Nitride Hybrids. *Nanomaterials*, 10(6): 1141, 2020.

[13] Rapoport, L., Fleischer, N., and Tenne, R. Applications of WS_2 (MoS_2) inorganic nanotubes and fullerene-like nanoparticles for solid lubrication and

for structural nanocomposites. *Journal of Materials Chemistry*, 15(18): 1782-1788, 2005.

[14] Kumar, R., Sahoo, S., Joanni, E., Singh, R. K., Yadav, R. M., Verma, R. K., Singh, D.P., Tan, W.K., Perez del Pino, A., Moshkalev, S.A., and Matsuda, A. A review on synthesis of graphene, h-BN and MoS_2 for energy storage applications: Recent progress and perspectives. *Nano Research*, *12*(11): 2655-2694., 2019.

[15] Xiao, J., Wang, X., Yang, X.Q., Xun, S., Liu, G., Koech, P.K., Liu, J. and Lemmon, J.P. Electrochemically induced high capacity displacement reaction of PEO/MoS_2/graphene nanocomposites with lithium. *Advanced Functional Materials*, 21(15): 2840-2846, 2011.

[16] Kumar, R., Sahoo, S., Joanni, E., Singh, R. K., Tan, W. K., Kar, K. K., and Matsuda, A. Recent progress in the synthesis of graphene and derived materials for next generation electrodes of high performance lithium ion batteries. *Progress in Energy and Combustion Science*, 75: 100786, 2019.

[17] Kumar, R., Sahoo, S., Joanni, E., Singh, R.K., Maegawa, K., Tan, W.K., Kawamura, G., Kar, K.K., and Matsuda, A. Heteroatom doped graphene engineering for energy storage and conversion. *Materials Today*, 39: 47-65, 2020.

[18] Tiwari, S. K., Sahoo, S., Wang, N., and Huczko, A. Graphene research and their outputs: Status and prospect. *Journal of Science: Advanced Materials and Devices*, 5(1): 10-29, 2020.

[19] Vikraman, D., Hussain, S., Truong, L., Karuppasamy, K., Kim, H.J., Maiyalagan, T., Chun, S.H., Jung, J., and Kim, H.S. Fabrication of MoS_2/WSe_2 heterostructures as electrocatalyst for enhanced hydrogen evolution reaction. *Applied Surface Science*, 480: 611-620, 2019.

[20] He, H. Y., He, Z., and Shen, Q. Efficient hydrogen evolution catalytic activity of graphene/metallic MoS_2 nanosheet heterostructures synthesized by a one-step hydrothermal process. *International Journal of Hydrogen Energy*, 43(48): 21835-21843, 2018.

[21] Groenendaal, L., Jonas, F., Freitag, D., Pielartzik, H., and Reynolds, J. R. Poly (3, 4-ethylenedioxythiophene) and its derivatives: past, present, and future. *Advanced materials*, 12(7): 481-494, 2000.

[22] Laforgue, A. All-textile flexible supercapacitors using electrospun poly (3, 4-ethylenedioxythiophene) nanofibers. *Journal of Power Sources*, 196(1): 559-564, 2011.

[23] Kelly, T. L., Yano, K., and Wolf, M. O. Supercapacitive properties of PEDOT and carbon colloidal microspheres. *ACS applied materials & interfaces*, 1(11): 2536-2543, 2009.

[24] Gupta, A., Arunachalam, V., and Vasudevan, S. Water dispersible, positively and negatively charged MoS_2 nanosheets: surface chemistry and the role of surfactant binding. *The journal of physical chemistry letters*, *6*(4): 739-744, 2015.

[25] Yu, H., Zhang, B., Bulin, C., Li, R., and Xing, R. High-efficient synthesis of graphene oxide based on improved hummers method. *Scientific reports*, *6*(1):1-7., 2016.

[26] Yoon, H., Chang, M., and Jang, J. Formation of 1D poly (3, 4-ethylenedioxythiophene) nanomaterials in reverse microemulsions and their application to chemical sensors. *Advanced Functional Materials*, 17(3): 431-436, 2007.

[27] Devi, M. and Kumar, A. In-situ reduced graphene oxide nanosheets–polypyrrole nanotubes nanocomposites for supercapacitor applications. *Synthetic Metals*, 222: 318-329, 2016.

[28] Huang, H. H., De Silva, K. K. H., Kumara, G. R. A., and Yoshimura, M. Structural evolution of hydrothermally derived reduced graphene oxide. *Scientific reports*, 8(1): 6849, 2018.

[29] Suvaci, E. and Özel, E. In *Encyclopedia of materials: technical ceramics and glasses*, volume 1, pages 59-68, Elsevier, 2021.

[30] Mungse, H. P., Sharma, O. P., Sugimura, H., and Khatri, O. P. Hydrothermal deoxygenation of graphene oxide in sub-and supercritical water. *RSC Advances*, 4(43): 22589-22595, 2014.

[31] Chutia, P., and Kumar, A. Charge carrier relaxation studies in poly (3, 4-ethylenedioxythiophene) nanofibers. *Journal of Polymer Research*, 22(6): 1-10, 2015.

[32] Zhao, Q., Jamal, R., Zhang, L., Wang, M., and Abdiryim, T. The structure and properties of PEDOT synthesized by template-free solution method. *Nanoscale research letters*, 9(1): 1-9, 2014.

[33] Cho, M. H., Ju, J., Kim, S. J., and Jang, H. Tribological properties of solid lubricants (graphite, Sb_2S_3, MoS_2) for automotive brake friction materials. *Wear*, *260*(7-8): 855-860, 2006.

[34] Sadhukhan, S., Ghosh, T.K., Rana, D., Roy, I., Bhattacharyya, A., Sarkar, G., Chakraborty, M., and Chattopadhyay, D. Studies on synthesis of reduced graphene oxide (RGO) via green route and its electrical property. *Materials Research Bulletin*, 79: 41-51, 2016.

[35] Fan, Z.J., Kai, W., Yan, J., Wei, T., Zhi, L.J., Feng, J., Ren, Y.M., Song, L.P., and Wei, F. Facile synthesis of graphene nanosheets via Fe reduction of exfoliated graphite oxide. *ACS nano*, *5*(1): 191-198, 2011.

[36] Selvaganesh, S.V., Mathiyarasu, J., Phani, K.L.N., and Yegnaraman, V.J.N.R.L. Chemical synthesis of PEDOT–Au nanocomposite. *Nanoscale Research Letters*, 2(11): 546-549, 2007.

[37] Wu, D., Zhang, J., Dong, W., Chen, H., Huang, X., Sun, B., and Chen, L. Temperature dependent conductivity of vapor-phase polymerized PEDOT films. *Synthetic metals*, 176: 86-91, 2013.

[38] Bagnall, A. G., Liang, W. Y., Marseglia, E. A., and Welber, B. Raman studies of MoS_2 at high pressure. *Physica B+ C*, 99(1-4): 343-346, 1980.

[39] Li, H., Zhang, Q., Yap, C. C. R., Tay, B. K., Edwin, T. H. T., Olivier, A., and Baillargeat, D. From bulk to monolayer MoS_2: evolution of Raman scattering. *Advanced Functional Materials*, 22(7): 1385-1390, 2012.

[40] Du, F.P., Cao, N.N., Zhang, Y.F., Fu, P., Wu, Y.G., Lin, Z.D., Shi, R., Amini, A., and Cheng, C. PEDOT: PSS/graphene quantum dots films with enhanced thermoelectric properties via strong interfacial interaction and phase separation. *Scientific reports*, 8(1): 1-12, 2018.

[41] Fabretto, M., Zuber, K., Hall, C., Murphy, P., and Griesser, H. J. The role of water in the synthesis and performance of vapour phase polymerised PEDOT electrochromic devices. *Journal of Materials Chemistry*, 19(42): 7871-7878, 2009.

[42] Khan, M. A., Armes, S. P., Perruchot, C., Ouamara, H., Chehimi, M. M., Greaves, S. J., and Watts, J. F. Surface characterization of poly (3, 4-ethylenedioxythiophene)-coated latexes by X-ray photoelectron spectroscopy. *Langmuir*, 16(9): 4171-4179, 2000.

[43] Mitraka, E., Jafari, M.J., Vagin, M., Liu, X., Fahlman, M., Ederth, T., Berggren, M., Jonsson, M.P., and Crispin, X. Oxygen-induced doping on reduced PEDOT. *Journal of Materials Chemistry A*, 5(9): 4404-4412, 2017.

[44] Bo, T., Wang, Y., Wang, J., Zhao, Z., Zhang, J., Zheng, K., Lin, T., Zhang, B., and Shao, L. Photocatalytic H_2 evolution on CdS modified with partially crystallized MoS_2 under visible light irradiation. *Chemical Physics Letters*, 746: 137305, 2020.

[45] Dong, H., Liu, C., Ye, H., Hu, L., Fugetsu, B., Dai, W., Cao, Y., Qi, X., Lu, H., and Zhang, X. Three-dimensional nitrogen-doped graphene supported molybdenum disulfide nanoparticles as an advanced catalyst for hydrogen evolution reaction. *Scientific reports*, 5(1): 1-11, 2015.

[46] Lin, T. W., Sadhasivam, T., Wang, A. Y., Chen, T. Y., Lin, J. Y., and Shao, L. D. Ternary composite nanosheets with MoS_2/WS_2/Graphene heterostructures as high performance cathode materials for supercapacitors. *Chem Electro Chem*, 5(7): 1024-1031, 2018.

[47] Johra, F. T., and Jung, W. G. Hydrothermally reduced graphene oxide as a supercapacitor. *Applied Surface Science*, 357: 1911-1914, 2015.

[48] Wang, C., Wang, S., Lv, J., Ma, Y., Zhou, G., Chen, M., Wang, Y., Zhao, M., and Chen, X. Effect of Ni doping on electrocatalytic hydrogen evolution activity of MoS_2. *International Journal of Electrochemical Science*, 14: 11607-11615, 2019.

[49] Qi, J., Jin, B., Bai, P., Zhang, W., and Xu, L. Template-free preparation of anthracite-based nitrogen-doped porous carbons for high-performance supercapacitors and efficient electrocatalysts for the oxygen reduction reaction. *RSC advances*, 9(42): 24344-24356, 2019.

[50] Gao, S., Li, X., Li, L., and Wei, X. A versatile biomass derived carbon material for oxygen reduction reaction, supercapacitors and oil/water separation. *Nano Energy*, 33: 334-342, 2017.

[51] Owens, D. K., and Wendt, R. C. Estimation of the surface free energy of polymers. *Journal of applied polymer science*, 13(8): 1741-1747, 1969.

[52] Annamalai, M., Gopinadhan, K., Han, S.A., Saha, S., Park, H.J., Cho, E.B., Kumar, B., Patra, A., Kim, S.W., and Venkatesan, T. Surface energy and wettability of van der Waals structures. *Nanoscale*, 8(10): 5764-5770, 2016.

[53] Kozbial, A., Li, Z., Sun, J., Gong, X., Zhou, F., Wang, Y., Xu, H., Liu, H., and Li, L. Understanding the intrinsic water wettability of graphite. *Carbon*, 74: 218-225, 2014.

[54] Mao, H., Lu, X., Chao, D., Cui, L., Li, Y., and Zhang, W. Preparation and characterization of PEDOT/β-Fe^{3+} O (OH, Cl) nanospindles with controllable sizes in aqueous solution. *The Journal of Physical Chemistry C*, 112(51): 20469-20480, 2008.

[55] Jang, J., Bae, J., and Park, E. Selective Fabrication of Poly (3, 4-ethylenedioxythiophene) Nanocapsules and Mesocellular Foams Using Surfactant Mediated Interfacial Polymerization. *Advanced Materials*, 18(3): 354-358, 2006.

[56] Liu, Y., Lin, S., Xu, Z., and Li, L. Morphology evolution and electrochemical properties of hierarchical $MoS_2/Co_3S_4/Ni_3S_4$ nanosheet-on-nanorod arrays. *Journal of Alloys and Compounds*, 814: 152269, 2020.

[57] Li, Q., Lu, W., Li, Z., Ning, J., Zhong, Y., and Hu, Y. Hierarchical $MoS_2/NiCo_2S_4$@C urchin-like hollow microspheres for asymmetric supercapacitors. *Chemical Engineering Journal*, 380: 122544, 2020.

[58] Karade, S. S., Dubal, D. P., and Sankapal, B. R. Decoration of ultrathin MoS_2 nanoflakes over MWCNTs: enhanced supercapacitive performance through electrode to symmetric all-solid-state device. *Chemistry Select*, 2(32): 10405-10412, 2017.

[59] Zheng, S., Fu, Y., Zheng, L., Zhu, Z., Chen, J., Niu, Z., and Yang, D. PEDOT-engineered Bi_2O_3 nanosheet arrays for flexible asymmetric supercapacitors with boosted energy density. *Journal of Materials Chemistry A*, 7(10): 5530-5538, 2019.

[60] Wang, J., Polleux, J., Lim, J., and Dunn, B. Pseudocapacitive contributions to electrochemical energy storage in TiO_2 (anatase) nanoparticles. *The Journal of Physical Chemistry C*, 111(40): 14925-14931, 2007.

[61] Chodankar, N.R., Pham, H.D., Nanjundan, A.K., Fernando, J.F., Jayaramulu, K., Golberg, D., Han, Y.K., and Dubal, D.P. True meaning of pseudocapacitors and their performance metrics: asymmetric versus hybrid supercapacitors. *Small*, 16(37): 2002806, 2020.

[62] Du, D., Lan, R., Xie, K., Wang, H., and Tao, S. Synthesis of $Li_2Ni_2(MoO_4)_3$ as a high-performance positive electrode for asymmetric supercapacitors. *RSC Advances*, 7(22): 13304-13311, 2017.

[63] Wang, J., Zhao, H., Xu, L., Yang, Y., He, G., and Du, Y. Three-Electron Redox Enabled Dithiocarboxylate Electrode for Superior Lithium Storage Performance. *ACS applied materials & interfaces*, 10(41): 35469-35476, 2018.

[64] Nie, S., Liu, L., Liu, J., Xie, J., Zhang, Y., Xia, J., Yan, H., Yuan, Y., and Wang, X. Nitrogen-doped TiO_2–C composite nanofibers with high-capacity and long-cycle life as anode materials for sodium-ion batteries. *Nano-micro letters*, 10(4): 1-13, 2018.

[65] Dong, X., Xu, H., Chen, H., Wang, L., Wang, J., Fang, W., Chen, C., Salman, M., Xu, Z., and Gao, C. Commercial expanded graphite as high-performance cathode for low-cost aluminum-ion battery. *Carbon*, 148: 134-140, 2019.

[66] Li, X., Zhang, C., Xin, S., Yang, Z., Li, Y., Zhang, D., and Yao, P. Facile synthesis of MoS_2/reduced graphene oxide@ polyaniline for high-performance supercapacitors. *ACS applied materials & interfaces*, 8(33): 21373-21380, 2016.

[67] Abraham, A.M., Lonkar, S.P., Pillai, V.V., and Alhassan, S.M. Three-Dimensional MoS_2 Nanodot-Impregnated Nickel Foam Electrodes for High-Performance Supercapacitor Applications. *ACS omega*, 5(20):11721-11729, 2020.

[68] Manuraj, M., Nair, K. K., Unni, K. N., and Rakhi, R. B. High performance supercapacitors based on MoS_2 nanostructures with near commercial mass loading. *Journal of Alloys and Compounds*, 819: 152963, 2020.

[69] Rajesh, M., Raj, C. J., Manikandan, R., Kim, B. C., Park, S. Y., and Yu, K. H. A high performance PEDOT/PEDOT symmetric supercapacitor by facile in-situ hydrothermal polymerization of PEDOT nanostructures on flexible carbon fibre cloth electrodes. *Materials today energy*, 6: 96-104, 2017.

[70] Wang, J., Li, Q., Peng, C., Shu, N., Niu, L., and Zhu, Y. To increase electrochemical performance of electrode material by attaching activated carbon particles on reduced graphene oxide sheets for supercapacitor. *Journal of Power Sources*, 450: 227611, 2020.

[71] Wang, Y., Zhang, W., Guo, X., Liu, Y., Zheng, Y., Zhang, M., Li, R., Peng, Z., Zhang, Y., and Zhang, T. One-step microwave-hydrothermal preparation of NiS/rGO hybrid for high-performance symmetric solid-state supercapacitor. *Applied Surface Science*, 514: 146080, 2020.

[72] Wu, H., He, D., and Wang, Y. Facile one-step process synthesized reduced graphene oxide/Mn_3O_4 nanocomposite for a symmetric supercapacitor. *Materials Letters*, 268: 127613, 2020.

[73] He, X., Yang, W., Mao, X., Xu, L., Zhou, Y., Chen, Y., Zhao, Y., Yang, Y., and Xu, J. All-solid state symmetric supercapacitors based on compressible and flexible free-standing 3D carbon nanotubes (CNTs)/poly (3, 4-ethylenedioxythiophene) (PEDOT) sponge electrodes. *Journal of Power Sources*, 376: 138-146, 2018.

[74] Rajesh, M., Manikandan, R., Kim, B. C., Becuwe, M., Yu, K. H., and Raj, C. J. Electrochemical polymerization of chloride doped PEDOT hierarchical porous nanostructure on graphite as a potential electrode for high performance supercapacitor. *Electrochimica Acta*, 136669, 2020.